

Dual elemental doping activated signaling pathway of angiogenesis and defective heterojunction engineering for effective therapy of MRSA-infected wounds

Jin Huang^{a,c,d}, Shuilin Wu^{a,d,*}, Yi Wang^{a,c,d}, Jie Shen^{b,**}, Chaofeng Wang^c, Yufeng Zheng^d, Paul K. Chu^e, Xiangmei Liu^{a,c,***}

^a Biomedical Materials Engineering Research Center, Hubei Key Laboratory of Polymer Materials, Ministry-of-Education Key Laboratory for the Green Preparation and Application of Functional Materials, School of Materials Science & Engineering, Hubei University, Wuhan, 430062, China

^b Shenzhen Key Laboratory of Spine Surgery, Department of Spine Surgery, Peking University Shenzhen Hospital, Shenzhen, 518036, China

^c School of Health Science & Biomedical Engineering, Hebei University of Technology, Tianjin, 300401, China

^d School of Materials Science & Engineering, Peking University, Beijing, 100871, China

^e Department of Physics and Department of Materials Science and Engineering, City University of Hong Kong, 999077, China

ARTICLE INFO

Keywords:

Methicillin-resistant *Staphylococcus aureus*
Defective heterojunction engineering
Wound healing
Phototherapy
Signaling pathways

ABSTRACT

Multi-drug resistant bacterial infections pose a significant threat to human health. Thus, the development of effective bactericidal strategies is a pressing concern. In this study, a ternary heterostructure (Zn–CN/P–GO/BiS) comprised of Zn-doped graphite phase carbon nitride (g-C₃N₄), phosphorous-doped graphene oxide (GO) and bismuth sulphide (Bi₂S₃) is constructed for efficiently treating methicillin-resistant *Staphylococcus aureus* (MRSA)-infected wound. Zn doping-induced defect sites in g-C₃N₄ results in a reduced band gap (ΔE) and a smaller energy gap (ΔE_{ST}) between the singlet state S₁ and triplet state T₁, which favours two-photon excitation and accelerates electron transfer. Furthermore, the formation of an internal electric field at the ternary heterogeneous interface optimizes the charge transfer pathway, inhibits the recombination of electron-hole pairs, improves the photodynamic effect of g-C₃N₄, and enhances its catalytic performance. Therefore, the Zn–CN/P–GO/BiS significantly augments the production of reactive oxygen species and heat under 808 nm NIR (0.67 W cm⁻²) irradiation, leading to the elimination of 99.60% ± 0.07% MRSA within 20 min. Additionally, the release of essential trace elements (Zn and P) promotes wound healing by activating hypoxia-inducible factor-1 (HIF-1) and peroxisome proliferator-activated receptors (PPAR) signaling pathways. This work provides unique insight into the rapid antibacterial applications of trace element doping and two-photon excitation.

1. Introduction

Bacterial invasion poses a formidable challenge in various public health domains, including food safety [1], medical care [2], and environmental sanitation [3]. Due to the rapid proliferation of bacteria, bacterial invasion can lead to persistent infection and complications [4]. Antibiotics are by far the most common and effective response to bacterial infections [5]. However, the overuse or misuse of traditional

antibiotics for bacterial infections has led to the emergence of antibiotic resistance and superbugs [6,7]. Therefore, it is imperative to develop a novel and efficacious antibacterial agent as an alternative to antibiotics for treating bacterial infections [8]. In recent decades, nanomaterials have been utilized as antibacterial agents using various methods [9,10]. Photo-responsive antibacterial nanomaterials are promising due to their low cost, environmental friendliness and universality [11,12]. Inorganic semiconductor materials, such as copper sulphide [13], bismuth

Peer review under responsibility of KeAi Communications Co., Ltd.

* Corresponding author. Biomedical Materials Engineering Research Center, Hubei Key Laboratory of Polymer Materials, Ministry-of-Education Key Laboratory for the Green Preparation and Application of Functional Materials, School of Materials Science & Engineering, Hubei University, Wuhan, 430062, China.

** Corresponding author. Shenzhen Key Laboratory of Spine Surgery, Department of Spine Surgery, Peking University Shenzhen Hospital, Shenzhen, 518036, China.

*** Corresponding author. School of Health Science & Biomedical Engineering, Hebei University of Technology, Tianjin, 300401, China.

E-mail addresses: slwu@pku.edu.cn (S. Wu), jayjayson909@gmail.com (J. Shen), liuxiangmei@hebut.edu.cn (X. Liu).

<https://doi.org/10.1016/j.bioactmat.2024.03.011>

Received 16 February 2024; Received in revised form 5 March 2024; Accepted 8 March 2024

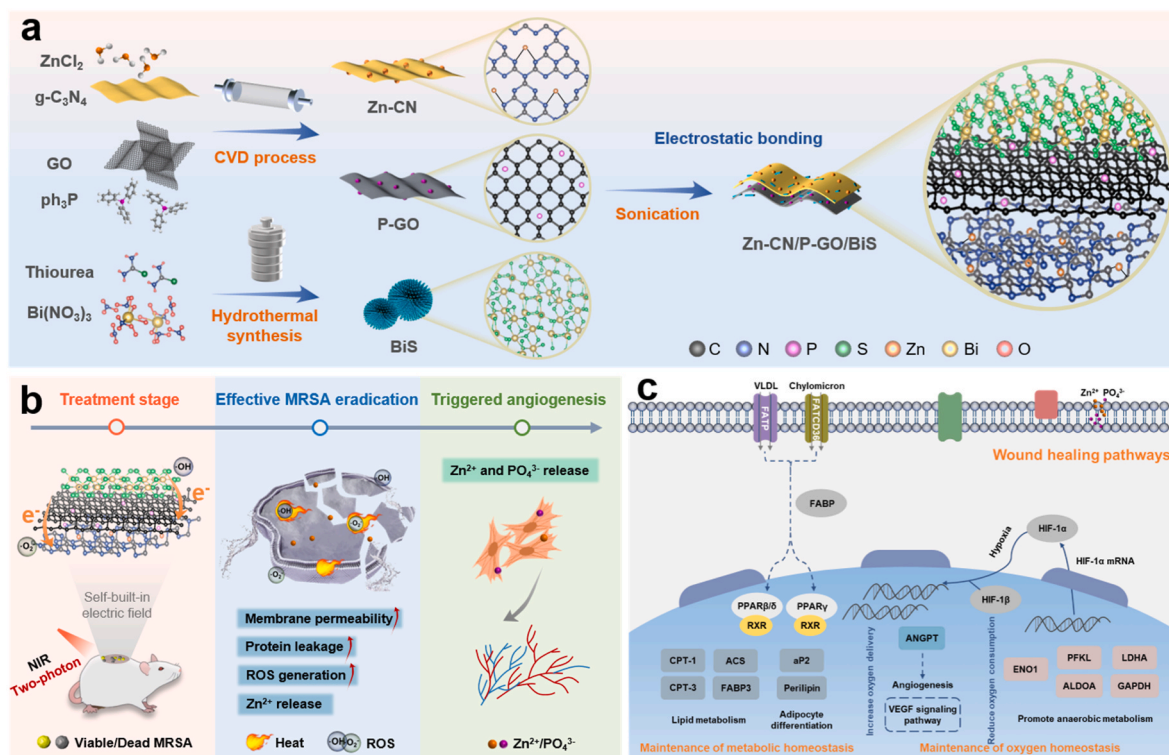
Available online 14 March 2024

2452-199X/© 2024 The Authors. Publishing services by Elsevier B.V. on behalf of KeAi Communications Co. Ltd. This is an open access article under the CC BY-NC-ND license (<http://creativecommons.org/licenses/by-nc-nd/4.0/>).

sulphide (Bi_2S_3) [14,15], molybdenum sulphide [16,17], black phosphorus [18,19] and graphene oxide (GO) [20,21] with photo-responsive properties, have been extensively studied by researchers. These materials can use solar energy to generate various reactive oxygen species (ROS) (such as hydroxyl radical [$\bullet\text{OH}$], superoxide anion [$\bullet\text{O}_2^-$], singlet oxygen [$^1\text{O}_2$], etc., by oxidized phospholipids, proteins, etc.) [22], which can effectively destroy bacterial cell membranes and disrupt normal bacterial metabolism [23]. Thus, they have sterilization purposes.

Graphite phase carbon nitride (g- C_3N_4 , hereafter, referred to as CN) is commonly used in light-driven photocatalytic water splitting and organic pollutant degradation due to its appropriate band gap width (~ 2.7 eV) and excellent biocompatibility [24]. Bi_2S_3 , hereafter, referred to as BiS, is a biosafe material [25]. Although BiS can generate ROS by producing electrons and holes under near-infrared (NIR) light, its narrow band gap (1.3–1.7 eV) leads to rapid recombination of separated electron-hole pairs [26], rendering it unsuitable for stand-alone photocatalytic reactions. By forming a heterogeneous interface with CN, the band gap of CN can be regulated while accelerating the transmission of photogenerated electrons and effectively separating electron-hole pairs [27]. GO is a zero-band gap material. As an excellent conductor, GO exhibits favourable photothermal properties and facilitates directional movement of photogenerated electrons in heterostructure [28]. This approach significantly enhances the photocatalytic performance of the composite. Elemental doping was used to construct defect sites [29,30]. Zn is an essential trace element in the human body, where it exists in many enzymes and genetic material [31]. It plays an extremely important role in human growth and development and in immunity and metabolism [32,33]. The antibacterial effect of Zn ions has been widely exploited in the field of nanomaterials [34]. Zn ions can bind to the bacterial cell membrane and membrane proteins, destroy membrane structure [35], damage the enzymes of the membrane electron transport system after entering cells and react with DNA [36]. Another important physiological element, P, is present in all cells of the human body and is involved in almost all physiological chemical reactions. In addition, P is

an important substance for maintaining the acid-base balance in the body and genetic substances transfer [37], participating in energy metabolism in the body [38] and affecting cell membrane permeability [39]. The construction of Zn and P doped defect sites can reduce the band gap [40,41], enhance the photocatalytic performance of composite materials that possess biological functions. Two-element doping has a higher band gap width regulation [42], which can regulate photocatalysis in multiple dimensions and also change the photothermal properties of the composite structure [43]. The construction of the ternary heterogeneous interface of Zn-CN/P-GO/BiS significantly improves the photocatalytic efficiency of the material and rapidly kills bacteria through a photothermal effect, a photodynamic effect and ion release [44,45], thereby promoting the repair and regeneration of infected wound tissue. The preparation process of Zn-CN/P-GO/BiS ternary heterojunction is depicted in Scheme 1a. The antimicrobial activity and repair mechanism of methicillin-resistant *Staphylococcus aureus* (MRSA)-infected wounds *in vivo* were described in Scheme 1b. Zn-CN/P-GO/BiS had an excellent antibacterial effect two-photon excitation under NIR irradiation. At the same time, Zn and P doped can upregulate angiogenesis and collagen production genes of fibroblasts, such as vascular endothelial growth factor (VEGF), basic fibroblast growth factor (bFGF), hypoxia-inducible factor-1 α (HIF-1 α), and collagen type III (COL-III), effectively promote the healing of wounds caused by bacterial infection. Proteomics analysis in Scheme 1c showed that it promoted angiogenesis by upregulating the expression of angiogenic proteins in the hypoxia-inducible factor-1 (HIF-1) signaling pathway, while upregulating proteins related to anaerobic metabolism and maintaining oxygen homeostasis in the wound. In addition, it also plays an important role in wound healing by upregulating a variety of adipocyte differentiation, lipid metabolism, and inflammatory response related proteins in the peroxisome proliferator-activated receptors (PPAR) signaling pathway, promoting the proliferation and differentiation of keratinocytes, and the keratinization of epidermis.



Scheme 1. (a) The synthesis process of Zn-CN/P-GO/BiS. (b) The synergistic antibacterial mechanisms under two-photon excitation and (c) the mechanisms of promoting angiogenesis.

2. Experimental methods

2.1. Preparation of Zn–CN, P-GO, BiS, Zn–CN/P-GO, Zn–CN/BiS, and Zn–CN/P-GO/BiS

The synthesis method was in accordance with that described in previous reports. Initially, CN powder was synthesized via chemical vapor deposition: 10 g of urea were placed in a porcelain boat and heated to 550 °C at a heating rate of 5 °C min⁻¹ for 2 h. Then, 0.1 g of yellow CN powder was prepared, with 0.1 g of CN dispersed in 10 mL of ethanol and heated to 80 °C, with constant stirring. Next, 0.02 g of ZnCl₂ was introduced, along with a few drops of 0.1 M hydrochloric acid to prevent the hydrolysis of Zn²⁺. After complete removal of ethanol, the sample was dried at 60 °C and subsequently ground before being placed in a porcelain boat. The sample was then heated in a tube furnace under a nitrogen atmosphere at a rate of 5 °C min⁻¹ until reaching 400 °C, where it was stored for 4 h. After cooling, the resulting Zn–CN was obtained by grinding.

First, 0.1 g of GO was dispersed in 30 mL of ethanol solution via ultrasonic treatment, followed by the addition of 0.1 g of triphenylphosphine for further sonication. The resulting mixture was subsequently dried at a temperature of 60 °C and then subjected to tube furnace annealing under a nitrogen atmosphere with a heating rate of 5 °C min⁻¹ until reaching a final temperature of 700 °C for 30 min. Finally, the sample was cooled and ground to obtain P-doped GO (P-GO).

A mixture of 0.2 g of bismuth nitrate and 1.0 g of thiourea was added to 50 mL of deionized water, stirred for 30 min and introduced into a reactor. The resulting solution was then heated to a temperature of 180 °C in a muffle furnace for 24 h, followed by centrifugation and washing with deionized water and absolute ethanol for precipitation purposes. Finally, the product was dried at a temperature of 60 °C for another 24 h before being ground to obtain BiS.

Zn–CN and P-GO were mixed in deionized water at a mass ratio of 8:2, followed by ultrasonic stripping for 12 h. After undergoing centrifugation and vacuum drying at 60 °C for 24 h, the Zn–CN/P-GO composite material was successfully obtained. The preparation method of Zn–CN/BiS composite material is the same as above.

A mixture of Zn–CN, P-GO, and BiS in deionized water at a mass ratio of 8:1:1 was subjected to ultrasonic stripping for 12 h. After centrifugation and vacuum drying at 60 °C for 24 h, the Zn–CN/P-GO/BiS composite was obtained.

2.2. Characterization

Field emission scanning electron microscopy (FE-SEM) (ZEISS Sigma 500; ZEISS, Germany) was utilized to examine the morphology and microstructure of the samples. Transmission electron microscopy (TEM) (FEI Talos F200X G2; Thermo Scientific, USA) images and energy dispersive X-ray (EDX) spectroscopy element mapping images were acquired. The compositions of the samples were analysed by X-ray photoelectron spectroscopy (XPS) (ESCALAB 250Xi; Thermo Scientific, USA). The phase structures were studied by The X-ray diffraction (XRD) (Bruker D8A A25; Bruker, Germany). The scanning range of the double diffraction angle spanned from 10° to 80°. The photothermal curves were measured, and images were taken by a thermal imager (FLIR E50; FLIR, USA). The potentials of the samples were measured by a particle size and Z potential analyser (Zetasizer Nano ZS90; Malvern Panalytical, UK). The photoluminescence (PL) spectra of the samples were determined by a fluorescence spectrometer (LS-55; PerkinElmer, USA). The UV–vis–NIR absorption spectra from 300 to 820 nm were determined by a UV–vis–NIR spectrophotometer (UV-3600; Shimadzu, Japan). Electron spin resonance (ESR) was determined using an electron paramagnetic resonance (EPR) spectrometer (Bruker EMXplus; Bruker, Germany). Fluorescence images were acquired using an inverted fluorescence microscope (Olympus IX73; Olympus, Japan), and

photocurrent density and electrochemical impedance spectroscopy (EIS) measurements were performed on an electrochemical workstation (CHI660E; Chen Hua Instrument, China). Ion release was determined by inductively coupled plasma optical emission spectroscopy (ICP-OES) (PQ9000; Jena, Germany).

2.3. Evaluation of photothermal effects

A uniform concentration (0.15 mg mL⁻¹) of each material solution was prepared, 200 μL was added to the 96-well plate, the light source was kept 3 cm away from the well plate, and the NIR was turned off after irradiation with 0.67 W cm⁻² of power for 20 min. Monitor the cooling temperature every minute until the ambient temperature was reached. This process was repeated three times.

The photothermal conversion efficiency (η) of Zn–CN/P-GO/BiS was calculated from the following equation (1):

$$\eta = \frac{hST_{\max} - T_0 - Q}{I(1 - 10^{-A})} \quad (1)$$

where H represents the heat transfer coefficient, S denotes the surface area of the container, T_{\max} signifies the maximum equilibrium temperature during heating, T_0 refers to the ambient temperature, Q represents the heat absorption rate of a 1.5 mL polystyrene centrifuge tube, I represents near-infrared power at 808 nm, and A indicates absorbance of Zn–CN/P-GO/BiS at 808 nm. During the cooling process, the time constant (τ_s) of Zn–CN/P-GO/BiS was determined using equation (2):

$$t = -\tau_s \ln \theta = -\tau_s \ln \frac{T - T_0}{T_{\max} - T_0} \quad (2)$$

Assuming equal heat absorption and release within the system, the photothermal conversion efficiency (η) was calculated by substituting equation (3) into equation (1), as below:

$$hS \approx \frac{m_{\text{H}_2\text{O}} - C_{\text{H}_2\text{O}}}{\tau_s} \quad (3)$$

where m represents the mass of water, and $C_{\text{H}_2\text{O}}$ denotes its specific heat capacity.

2.4. Evaluation of photoelectrochemical properties

The samples (3 mg mL⁻¹) was placed on conductive glass and dried, followed by an electrochemical test at an electrochemical workstation. A platinum electrode was used as the anti-electrode, and the reference electrode was an Ag/AgCl electrode. The sample groups were used as the working electrode, and 0.5 M Na₂SO₄ solution was used as the electrolyte. The working electrode was obtained by dropping 200 μL of sample solution onto conductive glass and drying thoroughly at room temperature. The photocurrent density and electrochemical impedance of different samples were then determined under NIR treatment (0.67 W cm⁻²).

2.5. ROS detection of materials

In this experiment, a mixture of 5 μL of 2',7'-dichlorodihydrofluorescein diacetate (DCFH-DA), 45 μL of absolute ethanol and 200 μL of 0.01 M NaOH was shaken in the dark for 30 min. Subsequently, a dilute solution was formed by adding 1 mL of phosphate-buffered saline (PBS), which was mixed with the sample solution to achieve a final concentration of 0.15 mg mL⁻¹. Following NIR irradiation, the fluorescence intensity of 2',7'-dichlorofluorescein (DCF) was measured after 0, 5, 10, and 15 min using a microplate reader.

2.6. In vitro antibacterial experiments

A bacterial suspension (100 μL) of MRSA, diluted to a concentration

of $\sim 2 \times 10^7$ CFU mL⁻¹ (CFU represents colony forming unit) in liquid medium, was mixed with 100 μ L of the sample solution in a 96-well plate. The final concentration of the prepared sample was 0.15 mg mL⁻¹. The bacterial mixture was exposed to NIR irradiation for 20 min. Subsequently, 10 μ L of the irradiated bacterial suspension was diluted by a factor of 400 and coated onto LB agar plates. The control group consisted of the bacterial solution without any sample. Antibacterial efficacy was determined based on the spread plate results using the following formula:

$$\text{Antibacterial efficiency (\%)} = \frac{CFU_{\text{control}} - CFU_{\text{sample}}}{CFU_{\text{control}}} \times 100\%.$$

2.7. Bacterial morphology and structure

Bacterial morphology and structure were observed using FE-SEM. Following the antibacterial experiment, the bacteria solution was allowed to stand for 1 h before discarding 160 μ L of the supernatant. The sample was then fixed in a dark environment with 2.5% glutaraldehyde for 2 h and washed several times with PBS. Subsequently, Gradient dehydration was performed using ethanol solutions of varying concentrations (30%, 50%, 70%, 90%, and 100%). After thorough drying, the bacteria were observed by FE-SEM.

2.8. Fluorescence staining of live and dead bacteria

To facilitate a more intuitive observation of bacterial survival or mortality status, Live & Dead Bacterial Staining Kit (Yeasen Biotech, China) was used to determine bacterial survival and mortality status. At the conclusion of the antibacterial experiment, 100 μ L of bacterial suspension were mixed with 1 μ L of working solution (1 μ L of DMAO, 2 μ L of EthD-III, and 8 μ L of normal saline). Subsequently, fluorescence images were captured using an inverted fluorescence microscope after thorough drying.

2.9. Membrane permeability and protein leakage

Isopropyl β -D-thiogalactopyranoside (IPTG) and *o*-nitrophenyl- β -D-galactoside (ONPG) (Beyotime, China) were utilized in membrane permeability test. Bacterial suspensions were incubated with IPTG for 12 h prior to centrifugation at 5000 rpm for 5 min and subsequently washed multiple times with PBS. The bacteria were then diluted to an optical density (OD) of approximately 0.08 at 600 nm using a microplate reader. The bacterial suspension mentioned above was combined with the sample solution and exposed to NIR irradiation. Subsequently, 15 μ L of irradiated supernatant were mixed with an ONPG working solution consisting of 15 μ L of 12.5 mM ONPG, 100 μ L of PBS, and 10 μ L of dimethylsulfoxide (DMSO). The OD value was measured at a wavelength of 420 nm. An Enhanced BCA (disodium 2, 2-biquinoline-4, 4-dicarboxylic acid) Protein Assay Kit (Beyotime, China) was utilized for the detection of MRSA protein leakage. The bacterial suspension was centrifuged at 5000 rpm for 5 min and subsequently washed with PBS multiple times to achieve a dilution of bacteria with an OD₆₀₀ value of approximately 0.08. The aforementioned bacterial suspension was then combined with the sample solution and subjected to irradiation, as in the antibacterial experiment. Finally, 25 μ L of supernatant obtained from centrifugation were mixed with 200 μ L of BCA working solution (solution A to solution B, ratio = 50:1) for 30 min before measuring its OD value at a wavelength of 562 nm.

2.10. Intracellular ROS determination

In this experiment, an ROS Assay Kit (Beyotime, China) was used to detect intracellular ROS levels. First, a bacterial solution (2 mL) was diluted to $\sim 2 \times 10^7$ CFU mL⁻¹ and incubated with 2 μ L of DCFH-DA at 37 °C for 30 min in darkness on a shaker. Subsequently, 100 μ L of the

aforementioned bacterial suspension was mixed with an equal volume of sample solution and exposed to NIR irradiation for 20 min. The resulting mixture was then centrifuged at 3000 rpm for 5 min, and a 20 μ L aliquot of the supernatant was stored in darkness for 1–2 days prior to imaging using an inverted fluorescence microscope after thorough drying.

2.11. Ion release test

The material was placed in a dialysis bag, and the release trend of Zn²⁺ and PO₄³⁻ from the material was tested at 37 °C. 3 mL of material (2 mg mL⁻¹) were immersed in a total volume of 30 mL of normal saline solution. After 0, 2, 5, 8, and 12 days, 3 mL of ion release solution was collected, and the same 3 mL of normal saline solution were re-added. The leaching concentrations of Zn²⁺ and PO₄³⁻ were detected by ICP-OES.

2.12. In vitro cell toxicity

The cytotoxicity of the sample solution against NIH 3T3 cells was assessed using an MTT assay. First, the cells were seeded onto a 96-well plate and allowed to adhere for 24 h before removal of dulbecco's modified eagle medium (DMEM). The sample solution was then diluted to 0.15 mg mL⁻¹ with DMEM, and 200 μ L of the solution were added to each well. After co-culturing with the cells for 1–3 days, the medium was discarded, and 200 μ L of 0.5 mg mL⁻¹ MTT solution were added. The cells were then incubated at 37 °C for 4 h. After discarding the MTT solution, 200 μ L of DMSO were added and shaken well. Following standing for 1 h, 100 μ L of supernatant were collected, and the OD values were measured at either 490 nm or 570 nm.

$$\text{Cell viability (\%)} = \frac{OD_{\text{sample}}}{OD_{\text{control}}} \times 100\%.$$

2.13. Cell morphology

To assess the growth status of the cells, fluorescence imaging was performed using 4',6-diamidino-2-phenylindole (DAPI) (Yeasen Biotech, China) staining solution and fluorescein isothiocyanate isomer (FITC) (Yeasen Biotech, China) was conducted. First, the cells were allowed to adhere to a 96-well plate for 24 h. DMEM was then removed and replaced with a sample solution diluted to 0.15 mg mL⁻¹ in DMEM, with 200 μ L of the solution placed in each well. Following co-culture with the cells for 24 h, the medium was gently aspirated and rinsed twice with an equal volume of PBS. Subsequently, 200 μ L of a 4% aqueous formaldehyde solution for fixation purposes were input into each well. After 10 min, the formaldehyde solution was removed by aspiration and washed twice with PBS, 10 min each time. Subsequently, 100 μ L of FITC diluted to a concentration of 1:1000 were added to the wells of a 96-well plate. Following a dark incubation period of 30 min, the wells were washed twice with PBS. Finally, DAPI diluted to a concentration of 1:100 was added to each well and allowed to stain for 30 s before being washed three times with PBS. Following storage in a dark environment and thorough desiccation, fluorescent imaging was conducted using an inverted fluorescence microscope.

2.14. Haemolysis assay

For the haemolysis assay, freshly drawn rat blood was subjected to refrigerated centrifugation at 3000 rpm for 15 min to obtain the underlying erythrocyte. This underlying erythrocyte was subsequently washed three times with normal saline and dispersed in a 5% concentration of the same solution. A mixture of diluted blood and each group of materials in a ratio of 1:1 were then incubated at 37 °C for 4 h before being centrifuged again at 3000 rpm for another 15 min using a refrigerated centrifuge. The supernatant was collected, and the OD value was measured at 570 nm. Deionized water served as a positive control,

and normal saline served as a negative control. The haemolysis rate (RHR%) of the samples was calculated using the following formula:

$$\text{RHR} (\%) = \frac{A_{\text{sample}} - A_{\text{normal saline}}}{A_{\text{water}} - A_{\text{normal saline}}} \times 100\%.$$

2.15. Cell scratch assay

First, 1 mL of cell suspension was added to a 24-well plate for adherent growth for 24 h. A line was then drawn along the middle using a 1 mL pipette tip perpendicular to the bottom of the well plate, and the cells were washed with PBS. Subsequently, the cells and materials of each group were co-cultured in DMEM for 0, 1, and 3 days. The migration of cells at different time points was observed using an inverted microscope.

2.16. qRT-PCR test

Cell suspension (2 mL) was added to a 6-well plate, and the cells were allowed to grow for 24 h. The medium was then changed, and the cells and materials of each group were co-cultured in DMEM for 5 days. The RNA content in a 10 μL reverse transcription system was made 500 ng, and cDNA was subsequently obtained by reverse transcription using PrimeScript RT Master Mix (Takara, China). The reference gene glyceraldehyde phosphate dehydrogenase (*GAPDH*) was used to normalize the relative expression of the other genes. The obtained cDNA was used as a qRT-PCR template for five genes (*GAPDH*, *VEGF*, *bFGF*, *HIF-1 α* , and *COL-III*). A CFX Connect Real-time PCR detection system (Bio-Rad, USA) was used for real-time fluorescence quantitative detection. 6 replicates and independent tests were performed for each group. In Table S1, we summarize the primer sequences.

2.17. In vivo animal experiments

A total of 27 male Sprague-Dawley rats weighing 150–200 g used in the animal experiments were procured from the Hubei Provincial Centre for Disease Control and Prevention. The Department of Orthopaedics at Union Hospital, Tongji Medical College, Huazhong University of Science and Technology approved the animal experiments. The animal experiment procedures were performed in accordance with the Animal Management Rules of the Ministry of Health of the P. R. of China and the Guidelines for the Care and Use of Laboratory Animals of China. The rats were randomly allocated into three groups: control, 3 M, and Zn–CN/P-GO/BiS. Following anaesthesia, a 6 mm diameter incision was made on the back skin of each rat, and an infection model was established by adding 10 μL of sample solution (0.15 mg mL⁻¹) and 10 μL of MRSA ($\sim 2 \times 10^7$ CFU mL⁻¹). The Zn–CN/P-GO/BiS group was exposed to NIR for 20 min, following which the wound healing was photographed at intervals of 2, 5, 8, and 12 days. On the second day, one-fourth of the wound tissue was extracted and placed in a culture medium (1 mL). Subsequently, bacterial spread plate count was conducted. The wound tissue was then subjected to Gram staining on days 2 and 5. Routine blood tests and Haematoxylin-eosin (H&E) staining of the wound tissue were conducted on days 2, 5, and 12. On day 12, the heart, liver, spleen, lung and kidney of the rats were sliced with H&E staining to evaluate the biocompatibility of Zn–CN/P-GO/BiS.

2.18. Proteomic analysis

12 rats were divided into control and Zn–CN/P-GO/BiS groups. A hole punch with a diameter of 6 mm was used to punch holes on the back of the rats, and subsequently 20 μL of Zn–CN/P-GO/BiS solution at a concentration of 0.15 mg mL⁻¹ was added to the wound. The control group did not receive any treatment. The wound tissue was taken on day 12 and placed in the refrigerator at -80°C . Remove and grind in a liquid nitrogen mortar. Four times the powder volume of lysis buffer was

added and sonicated. The suspension was centrifuged at 12,000 rpm for 10 min at 4°C in a centrifuge, and the supernatant was determined by protein concentration using an Enhanced BCA Protein Assay Kit. Equal amounts of proteins from each group were subjected to trypsin digestion, and the peptides digested by trypsin were desalted with Strata X C18, followed by vacuum freeze drying. Peptides were labeled according to the operating instructions of the tandem mass tag label reagent (Thermo Fisher Scientific, USA). The peptides were dissolved by liquid chromatography with mobile phase A, separated by the EASY-nLC 1200 ultra-high performance liquid phase system, then injected into an NSI ion source for ionization, and finally analysed by Orbitrap Exploris 48 mass spectrometer.

2.19. Statistical analyses

Each experiment was repeated at least three times and all data were shown as means \pm SD. The paired or unpaired t-tests, one-way analysis of variance (ANOVA) and two-way ANOVA were used in statistical analyses. * $p < 0.05$, ** $p < 0.01$, *** $p < 0.001$, and **** $p < 0.001$. When $p > 0.05$, no significance was considered between groups (ns).

3. Results and discussion

3.1. Morphological structure

Field emission scanning electron microscopy (FE-SEM) showed that Zn–CN had a sheet structure, with no significant change in its morphology compared with that of CN (Fig. S1). Transmission electron microscopy (TEM) images of Zn–CN (Fig. S2) revealed an absence of discernible lattice fringes. Energy-dispersive X-ray (EDX) spectroscopic elemental mapping of Zn–CN (Fig. S3) indicated that the distribution of Zn was homogeneous throughout the sample. The thin-layer structure of GO (Fig. S4a), which shrinkage upon the addition of P due to calcination (Fig. S4b), exhibited a wrinkled morphology. Figs. S4c–S6 show its binding state after sonication with Zn–CN. FE-SEM images revealed that BiS possesses a flower-shape, rod-like structure (Fig. S7a). The combination of BiS and Zn–CN resulted in the formation of Zn–CN/BiS, which accumulated fine rod-like BiS and flaky Zn–CN (Figs. S7b–S8a), with lattice spacing of about 0.195 nm (Figs. S8b–c). This corresponded to the (431) crystal plane of BiS. Elemental mapping revealed that C, N, Zn, Bi, and S were uniformly distributed in the composite (Fig. S9). In terms of the structure of the synthesized Zn–CN/P-GO/BiS, TEM (Fig. 1a and Fig. S10) and FE-SEM (Fig. S11) images showed that it contained multiple layers of nanosheets and a limited quantity of nanorods. BiS exhibited lattice fringes at the (130) and (221) crystal planes (Fig. 1b). Fig. 1c–e showed the selected area electron diffraction (SAED) patterns of the corresponding area in Fig. 1a. Fig. 1c indicates that P-GO is amorphous, and Fig. 1d belongs to the spots of BiS on the (211), (130), (221), and (020) planes. Fig. 1e indicates that the amorphous Zn–CN area with a small amount of BiS, which belongs to the spots of BiS on the (200), (022), and (242) planes. EDS elemental mapping revealed an optimal distribution of all elements on Zn–CN/P-GO/BiS (Fig. 1f and Fig. S12), demonstrating successful synthesis of Zn–CN/P-GO/BiS. Fig. 1g indicates that the surface of Zn–CN/P-GO/BiS has several different functional groups, which strongly interact with cations. In the undoped CN structure, N atoms are easily bound to Zn ions through ionic bonds, which facilitates the formation of heterostructures.

The X-ray diffraction (XRD) analysis presented in Fig. S13 indicates that the diffraction peak observed at $2\theta = 27.4^\circ$ can be attributed to the (002) crystal planes of both CN and Zn–CN. The peak intensity was also reduced due to the interaction of CN with Zn ions, thus changing the pore structure and the hole-to-hole distance. GO exhibited a diffraction peak at $2\theta = 11.1^\circ$, with a crystal plane of (100). P-GO showed a significant diffraction peak at $2\theta = 25.9^\circ$, which was caused by the transition of the synthesized GO to graphene, and it belongs to the diffraction of the hexagonal graphite (002) crystal plane. BiS at $2\theta =$

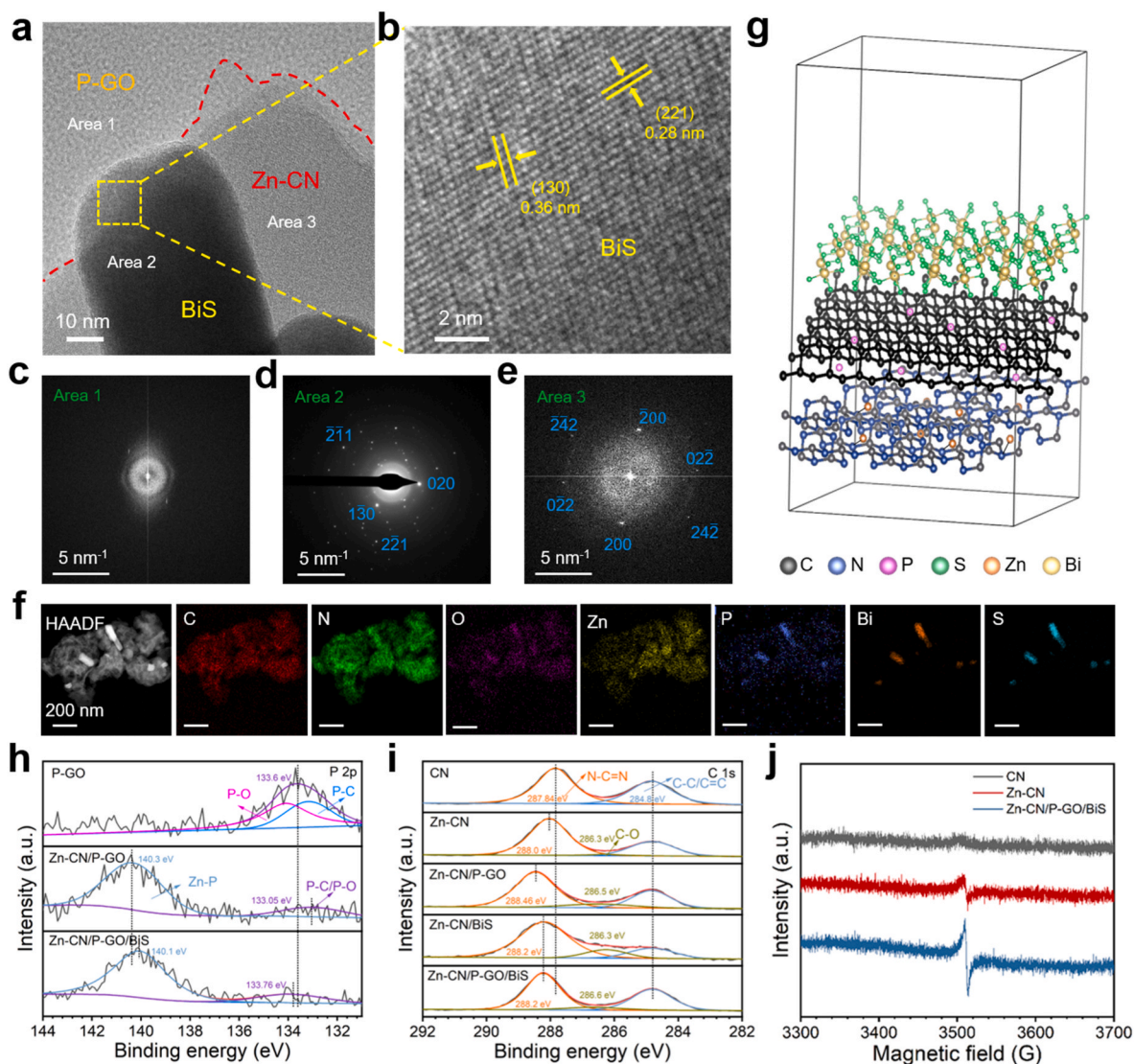


Fig. 1. Morphology and structural characterization. (a–b) TEM images of Zn-CN/P-GO/BiS. (c–e) SAED patterns for different area in (a). (f) EDX elemental mapping of Zn-CN/P-GO/BiS (scale bars, 200 nm). (g) Crystal structure of Zn-CN/P-GO/BiS. High-resolution XPS spectra of (h) P 2p and (i) C 1s. (j) EPR spectra of CN, Zn-CN, and Zn-CN/P-GO/BiS.

24.93°, 28.6°, and 31.79° corresponded to the (130), (211), and (221) crystal planes of BiS, respectively. The presence of these distinctive peaks in Zn-CN/P-GO/BiS confirmed the successful synthesis of a ternary composite comprising Zn-CN, P-GO, and BiS. As depicted in Fig. S14, CN exhibited a weak negative potential, whereas the potential of Zn-CN increased following Zn doping. Due to the presence of a hydrophilic carboxyl group in GO, the binding potential of Zn-CN to P-GO decreased. The addition of BiS decreased the binding potential. The chemical composition of the samples was analysed by X-ray photoelectron spectroscopy (XPS). According to the XPS data, the C-peak signal of Zn-CN/P-GO/BiS was enhanced after combination (Fig. S15). The spectra of CN, Zn-CN, GO, P-GO, Zn-CN/P-GO, BiS, Zn-CN/BiS, and Zn-CN/P-GO/BiS were all corrected using the C 1s peak at 284.8 eV. As shown in Fig. 1h, a new peak at 140.3 eV was found in the XPS spectrum of Zn-CN/P-GO, which was attributed to the Zn–P bond based on previous work by Wang et al. [46]. In Fig. 1i, the fitted peak of CN corresponds to the C 1s orbital 287.84 eV, Zn-CN corresponds to the C 1s orbital 288.0 eV, and Zn-CN/P-GO/BiS corresponds to the C 1s orbital 288.2 eV. This indicates that the C peak moved towards a higher binding energy after the material is a composite. In Fig. S16, the fitted peaks of N, Zn, and Bi also shifted to different degrees, and the binding energies

of the C–N–C, C–N=C, and N≡C, Zn 2p_{1/2} orbitals and Zn 2p_{3/2} orbitals in Zn-CN/P-GO/BiS increased, indicating that the binding energies of the inner electrons increased. The binding energies of the Bi 4f_{5/2} orbitals and Bi 4f_{7/2} orbitals in Zn-CN/P-GO/BiS were lower than those in the other groups, indicating that the binding energies of the inner electrons were smaller. We used electron paramagnetic resonance (EPR) spectroscopy to detect the intensity of oxygen vacancies (Fig. 1j). The results showed that the resonance peak intensities of Zn-CN/P-GO/BiS and Zn-CN were much stronger than the resonance peak intensity of CN, which confirmed the presence of higher concentrations of oxygen vacancies in the doped material.

3.2. Photoelectrochemical properties

UV–vis–NIR absorption tests were conducted at a concentration of 0.15 mg mL⁻¹, as illustrated in Fig. 2a. This outcome suggests that Zn-CN/P-GO/BiS exhibits superior absorption properties at 808 nm compared to the other groups. The photothermal properties of the materials were then investigated under 808 nm NIR (0.67 W cm⁻²) for 20 min. As depicted in Fig. 2b and the corresponding infrared thermal imaging photographs in Fig. S17, the Zn-CN/P-GO/BiS composite

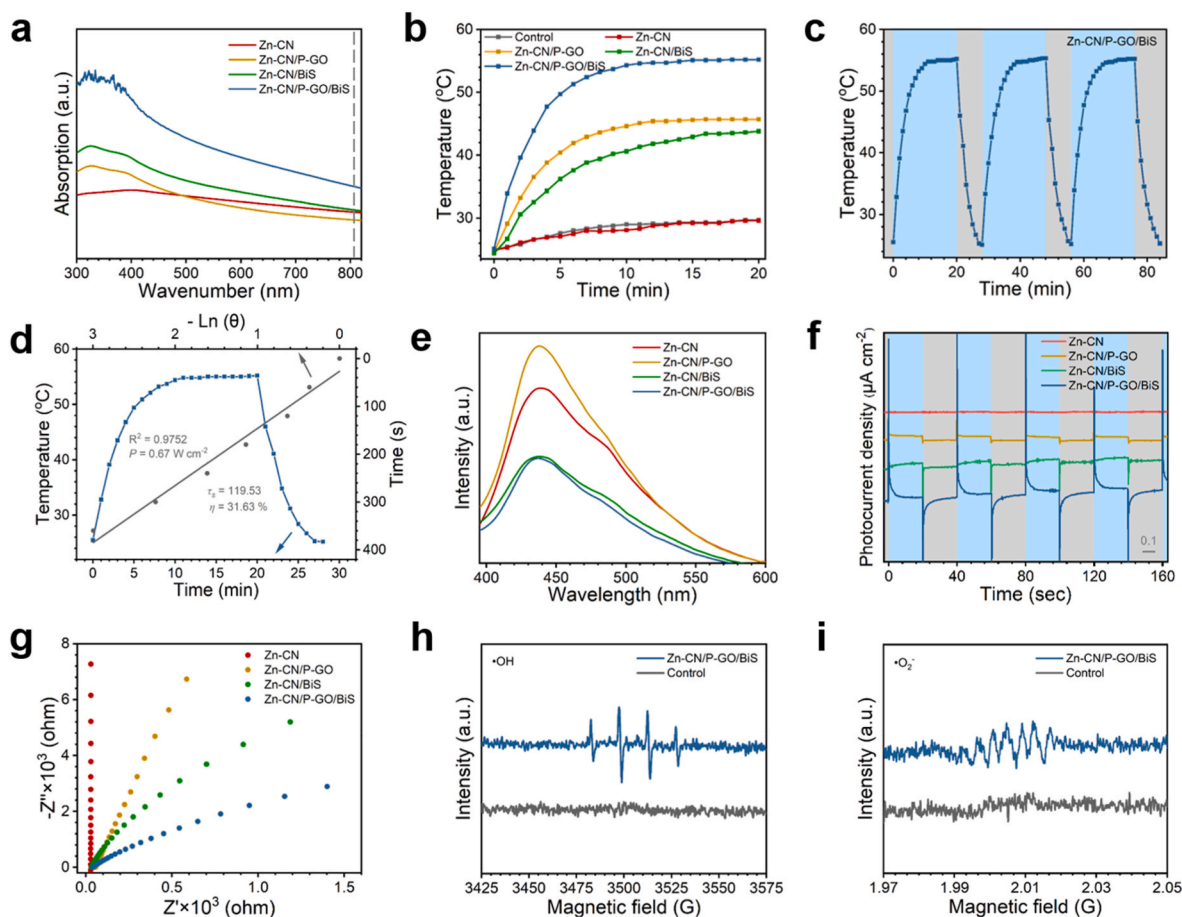


Fig. 2. Photoelectrochemical properties of Zn-CN/P-GO/BiS. (a) UV-vis-NIR absorption. (b) Photothermal curves of different materials. (c) Photothermal cycle curve of the Zn-CN/P-GO/BiS (3 cycles). (d) The photothermal conversion efficiency (η) of Zn-CN/P-GO/BiS at 808 nm was calculated. (e) PL spectra. (f) Photocurrent responses. (g) EIS. ESR spectra of (h) $\bullet\text{OH}$ and (i) $\bullet\text{O}_2^-$.

material (0.15 mg mL^{-1}) can attain a temperature as high as $55.2 \text{ }^\circ\text{C}$, which was significantly higher than that of the other groups ($29.7 \text{ }^\circ\text{C}$, $29.6 \text{ }^\circ\text{C}$, $45.7 \text{ }^\circ\text{C}$, and $43.8 \text{ }^\circ\text{C}$). This finding indicated that the Zn-CN/P-GO/BiS composite exhibited excellent photothermal properties. The Zn-CN/P-GO/BiS composite exhibited stable temperature changes, maintaining almost constant maximum temperatures over three cycles, as observed in an infrared irradiation switch cycle experiment (Fig. 2c), indicating its excellent and consistent photothermal performance. The closed phase of NIR was analysed through cycle curve calculation to obtain a linear regression curve (Fig. 2d). The results revealed photothermal conversion efficiency of 31.63%.

The photocatalytic performance of the material is influenced by the separation efficiency of photogenerated electron-hole pairs. Photoluminescence (PL) spectroscopy was used to assess the separation efficiency. The addition of P-GO and BiS effectively inhibited the recombination of charges, resulting in Zn-CN/P-GO/BiS exhibiting the lowest fluorescence intensity compared to that of the other groups, indicating that it had the highest photocatalytic efficiency (Fig. 2e). This finding was confirmed by the photocurrent response. As depicted in Fig. 2f, Zn-CN/P-GO/BiS exhibited significantly higher photocurrent response compared to the other groups during four successive NIR cycles. The photoelectrode current increases under light condition and decreases under off light condition, which proves that the change is driven by optical drive. The enhanced photocurrent indicated more efficient separation of photogenerated electron-hole pairs in the sample, which suppressed electron-hole recombination and thus enhanced its photodynamic capability. To further verify the photoelectric characteristics of Zn-CN/P-GO/BiS, we performed an impedance analysis

(Fig. 2g). Electrochemical impedance spectroscopy (EIS) data revealed the curvature radius decreases after heterojunction formation, indicating that doping promotes charge transfer. After the formation of heterojunction, steric hindrance decreases due to the improvement of charge transport at the heterojunction interface. Overall, the findings indicated that the addition of P-GO and BiS enhanced the photocatalytic efficiency of the heterojunction.

ROS generation for each group of materials was detected by the ROS fluorescent probe 2',7'-dichlorodihydrofluorescein diacetate (DCFH-DA) under NIR irradiation. After contact with ROS, DCFH-DA will be oxidized to 2',7'-dichlorofluorescein (DCF) and emits fluorescence. The results revealed that ROS production of Zn-CN/P-GO/BiS was higher than that of the other groups due to enhanced photocatalysis (Fig. S18), with 160.6 times more ROS generation in the Zn-CN/P-GO/BiS group compared to the control group due to the photodynamic effect. To determine the type of ROS generated, the electron spin resonance (ESR) signal was analysed using 5,5-dimethyl-1-pyrroline N-oxide as a trapping agent. A robust $\bullet\text{OH}$ (Fig. 2h) and $\bullet\text{O}_2^-$ (Fig. 2i) ESR signal was detected in the Zn-CN/P-GO/BiS group, whereas almost no signal was observed in the control group, also under NIR irradiation.

3.3. Photocatalytic mechanism and theoretical calculations

To assess the photodynamic properties of Zn-CN/P-GO/BiS, UV-vis-NIR diffuse reflectance spectroscopy (DRS) of various samples was conducted (Fig. 3a). Based on the DRS results, the band gap of each group of materials was calculated using the Kubelka-Munk function, as presented in Fig. 3b. All materials before contact, the band gap of BiS

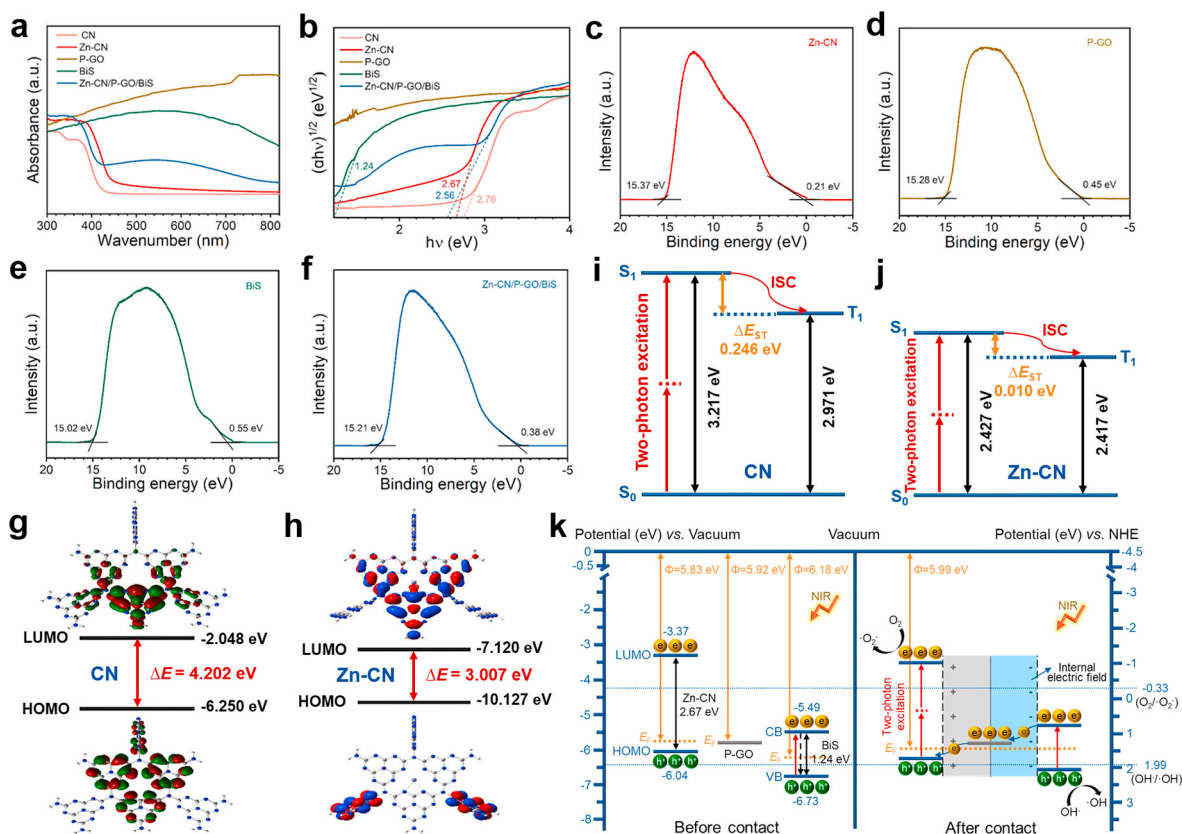


Fig. 3. Analysis of photocatalytic mechanism. (a) UV-vis-NIR diffuse reflectance spectra and (b) corresponding Kubelka-Munk function plots. UPS of (c) Zn-CN, (d) P-GO, (e) BiS, and (f) Zn-CN/P-GO/BiS. ΔE was calculated for (g) CN and (h) Zn-CN in dichloromethane. Calculated ΔE_{ST} of (i) CN and (j) Zn-CN. (k) Based on the work function and the band structure, the band diagram of Zn-CN, P-GO, and BiS before and after contact were calculated.

was approximately 1.24 eV, which was consistent with previously reported band gap values in the literature. Upon Zn doping, the absorption edge of CN was reduced from 2.76 eV to 2.67 eV due to an increase in vacancies caused by lattice defects. The incorporation of P-GO and BiS into Zn-CN further narrowed the energy gap to 2.56 eV, indicating that Zn-CN/P-GO/BiS has a higher photoexcitation efficiency compared to the other materials. Ultraviolet photoelectron spectroscopy (UPS) tests were conducted to determine the work functions (Φ) and secondary electron cut-off (E_c -cut-off) edges. As depicted in Fig. 3c–f, the E_c -cut-offs for Zn-CN, P-GO, BiS, and Zn-CN/P-GO/BiS were 15.37 eV, 15.28 eV, 15.02 eV, and 15.21 eV, respectively. After subtracting the excitation energy of He I (21.20 eV), the corresponding Φ were 5.83 eV, 5.92 eV, 6.18 eV, and 5.99 eV, respectively. Their highest occupied molecular orbitals (HOMOs)/valence bands (VBs) and lowest unoccupied molecular orbitals (LUMOs)/conduction bands (CBs) were calculated from the Φ and band structures, respectively. Based on density functional theory (DFT) calculations (the theoretical calculated values were greater than the real values), the HOMO-LUMO energy level difference ΔE of CN (4.202 eV) (Fig. 3g) was larger than that of Zn-CN (3.007 eV) (Fig. 3h), suggesting that doping made ΔE smaller and more conducive to the transition of molecules from the ground state (S_0) to the excited state (S_1) compared with pure CN. As shown in Fig. 3i and j, singlet S_1 in the excited state transitioned to a long-life excited triplet state through intersystem crossover (ISC) [47,48]. Doping with Zn reduced the energy gap (ΔE_{ST}) between the singlet and triplet states, making it easier for the S_1 state to be converted to the T_1 state and increasing the triplet T_1 formation rate [49].

According to the results of DFT and UPS, the catalytic mechanism was illustrated in Fig. 3k. As shown in the mechanism diagram, the spontaneous transfer of electrons occurred from larger to smaller Fermi energy (E_F), resulting in the formation of a space charge region [50].

Under NIR irradiation, the electron-hole pair of BiS was separated, and the photogenerated electrons were transferred from the VB of BiS to the CB, with the electrons concentrated on the CB and the holes concentrated on the VB. Due to the existence of the internal electric field, some of the photogenerated electrons concentrated on the CB of BiS were transferred to P-GO. This accelerated electron transfer, reduced the recombination of electrons and holes and left holes on the VB, which resulted in more holes and electrons to participate in the generation of hydroxyl radicals ($\bullet\text{OH}$). P-GO can act as a conductor to transfer electrons to the HOMOs of Zn-CN [51], from which electrons jump to LUMOs and react with oxygen and electrons to produce superoxide anions ($\bullet\text{O}_2^-$) [52,53]. This idea is supported by the finding that the VB (vs. vacuum) of BiS in Zn-CN/P-GO/BiS was lower than that of $\text{OH}^-/\bullet\text{OH}$ (1.99 eV) (vs. NHE), indicating the potential for electron-mediated conversion of oxygen to $\bullet\text{OH}$. The LUMOs (vs. vacuum) of Zn-CN were higher than $\text{O}_2/\bullet\text{O}_2^-$ (-0.33 eV) (vs. NHE), suggesting that oxygen can also be electronically converted to $\bullet\text{O}_2^-$ [54].

3.4. Exploration of the mechanism underlying the antibacterial efficacy

The antibacterial efficacy of each group of the materials was assessed through a spread plate test. As depicted in Fig. 4a and b and Fig. S19, the plate coated colony results, colony forming unit (CFU), and antibacterial ratios, respectively. When exposed to NIR (0.15 mg mL^{-1}) for 20 min, there was no significant change in the survival counts of MRSA in the Zn-CN group compared to that in the control group. The MRSA colonies of Zn-CN/P-GO/BiS treatment were significantly reduced, and the corresponding antibacterial ratio was $99.60\% \pm 0.07\%$. The antibacterial ratios in the Zn-CN/P-GO and Zn-CN/BiS groups were $60.66\% \pm 3.76\%$ and $72.49\% \pm 0.35\%$, respectively, both lower than the Zn-CN/P-GO/BiS group under identical conditions. The bacterial colony counts of the

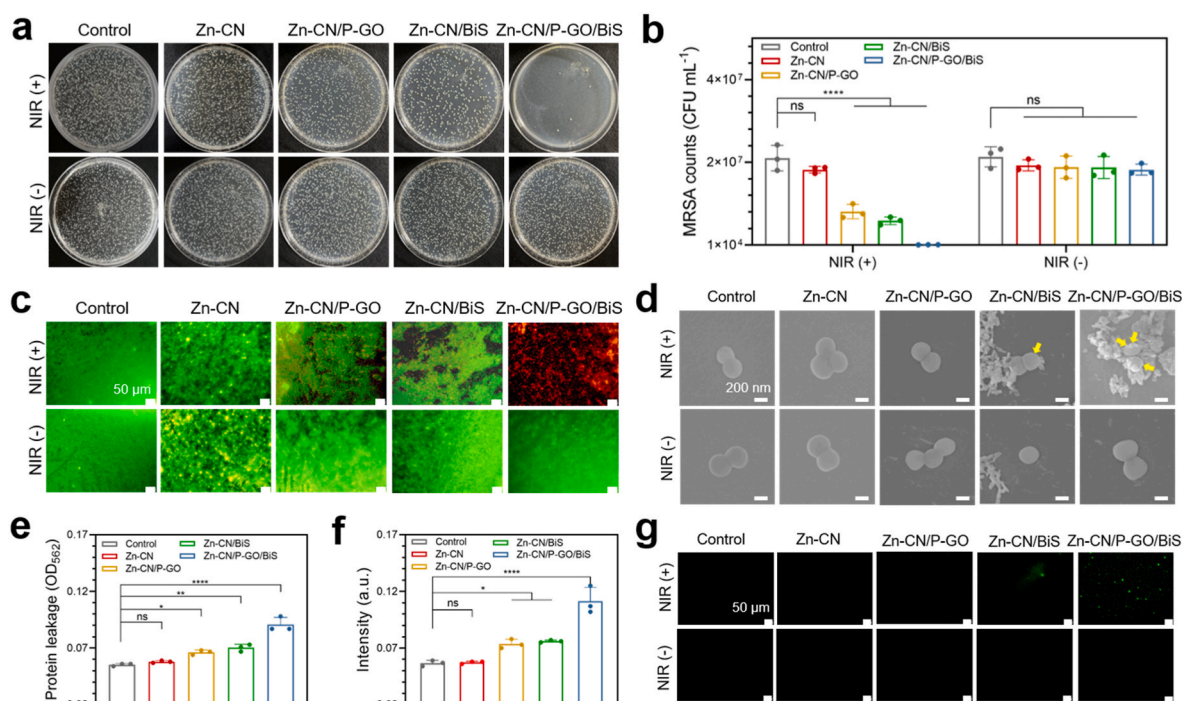


Fig. 4. Antibacterial tests *in vitro* and research on antibacterial mechanisms. (a) Spread plate results of MRSA in different materials after treatment irradiation with 808 nm NIR or in the dark for 20 min. (b) The corresponding MRSA counts of different materials. (c) Live-dead fluorescence staining of MRSA (scale bars, 50 nm). The green fluorescence signifies the presence of live bacteria, while the red fluorescence signifies the presence of dead bacteria. (d) FE-SEM images of MRSA morphology (scale bars, 200 nm). (e) Protein leakage of MRSA. (f) ONPG membrane permeability test. (g) Fluorescence staining images of MRSA treated by materials with DCFH-DA probe (scale bars, 50 μm).

dark control groups were almost identical after an incubation period of 20 min, indicating negligible antibacterial activity. To visually demonstrate the antibacterial efficacy of the materials, we conducted a live/dead fluorescence staining experiment on bacteria. As depicted in Fig. 4c, red fluorescence was detected in the Zn-CN/P-GO/BiS group, pointing to bacterial mortality, whereas minimal red fluorescence or predominantly green fluorescence was detected in the other groups, indicating the presence of live bacteria. Then we investigated the effect of materials in each group on the morphology of bacteria under NIR irradiation. As shown in Fig. 4d, bacterial morphology was normal in all the groups under dark conditions. After exposure to NIR for 20 min, the bacterial cell membrane in the Zn-CN/P-GO and Zn-CN/BiS groups exhibited only slight contraction, whereas the bacterial cell membrane in the Zn-CN/P-GO/BiS group (indicated by yellow arrows) displayed evident rupture and deformation. These findings suggested that NIR can accelerate the bactericidal effect of the material by rapidly disrupting the bacterial membrane.

When the bacterial membrane is disrupted, proteins are released. A protein leakage experiment (Fig. 4e) demonstrated that MRSA co-cultured with each group of materials exhibited increased protein leakage after NIR irradiation. Notably, the Zn-CN/P-GO/BiS group displayed the highest level of protein leakage. We verified its damaging effect on bacteria by measuring the permeability of the cell membrane of MRSA by *o*-nitrophenyl- β -D-galactoside (ONPG) hydrolysis (Fig. 4f). The experimental results indicated that there was no statistically significant difference between the control group and Zn-CN group, whereas the permeability of the Zn-CN/P-GO and Zn-CN/BiS groups exhibited a slight increase compared to that of the control group. The permeability of bacteria cell membrane was significantly enhanced in the Zn-CN/P-GO/BiS group, and the hydrolysis rate of ONPG was greatly accelerated in this group. These results demonstrated that the Zn-CN/P-GO/BiS group exhibited superior antibacterial efficacy through synergistic photothermal and photocatalytic effects. Excessive levels of ROS by bacteria can disrupt bacterial physiology, ultimately leading to bacterial

death [55], as shown by the staining of intracellular ROS using DCFH-DA (Fig. 4g). The results showed that after NIR irradiation, the Zn-CN/P-GO/BiS group exhibited the strongest green fluorescence, indicating the highest level of intracellular ROS production compared to that of the other groups, which showed little or no ROS production. In the absence of NIR, almost no green fluorescence was observed due to the absence of ROS production. This proves that the production of ROS in the material is driven by NIR light. Therefore, the DCFH-DA results suggested that the generation of ROS under the synergistic action of photothermal and photodynamic forces improved the antibacterial performance of Zn-CN/P-GO/BiS.

3.5. *In vitro* biocompatibility and fibroblasts proliferation-promoting behaviour

During the process of wound healing, the release of Zn and P stimulates the formation of epithelial cells, which has biological functions [56,57]. Fig. 5a and b showed the concentrations of Zn²⁺ and PO₄³⁻ released into normal saline solution by Zn-CN/P-GO/BiS at different times at 37 °C. The release rate of Zn²⁺ changed from fast to slow and was almost completed on the fifth day, while the release of PO₄³⁻ was almost completed on the second day, indicating that it was doped into the pores. To evaluate the cytocompatibility of the materials, we conducted a haemolysis assay (Fig. 5c and Fig. S20), which revealed that all the materials exhibited a haemolysis rate below 2%, indicating excellent biocompatibility. This finding pointed to low cytotoxicity of the materials.

Cell morphology is indicative of cell growth. To evaluate the effect of biological functional elements on cell proliferation, we divided all groups into ion-free (control, CN), single-ion (Zn-CN and P-GO), and double-ion (Zn-CN/P-GO/BiS) groups. Visualization of fibroblasts fluorescence staining (Fig. S21) revealed that compared to the control group, the survival rates in the CN and Zn-CN groups were reduced, and cellular proliferation was impaired. Conversely, the other groups

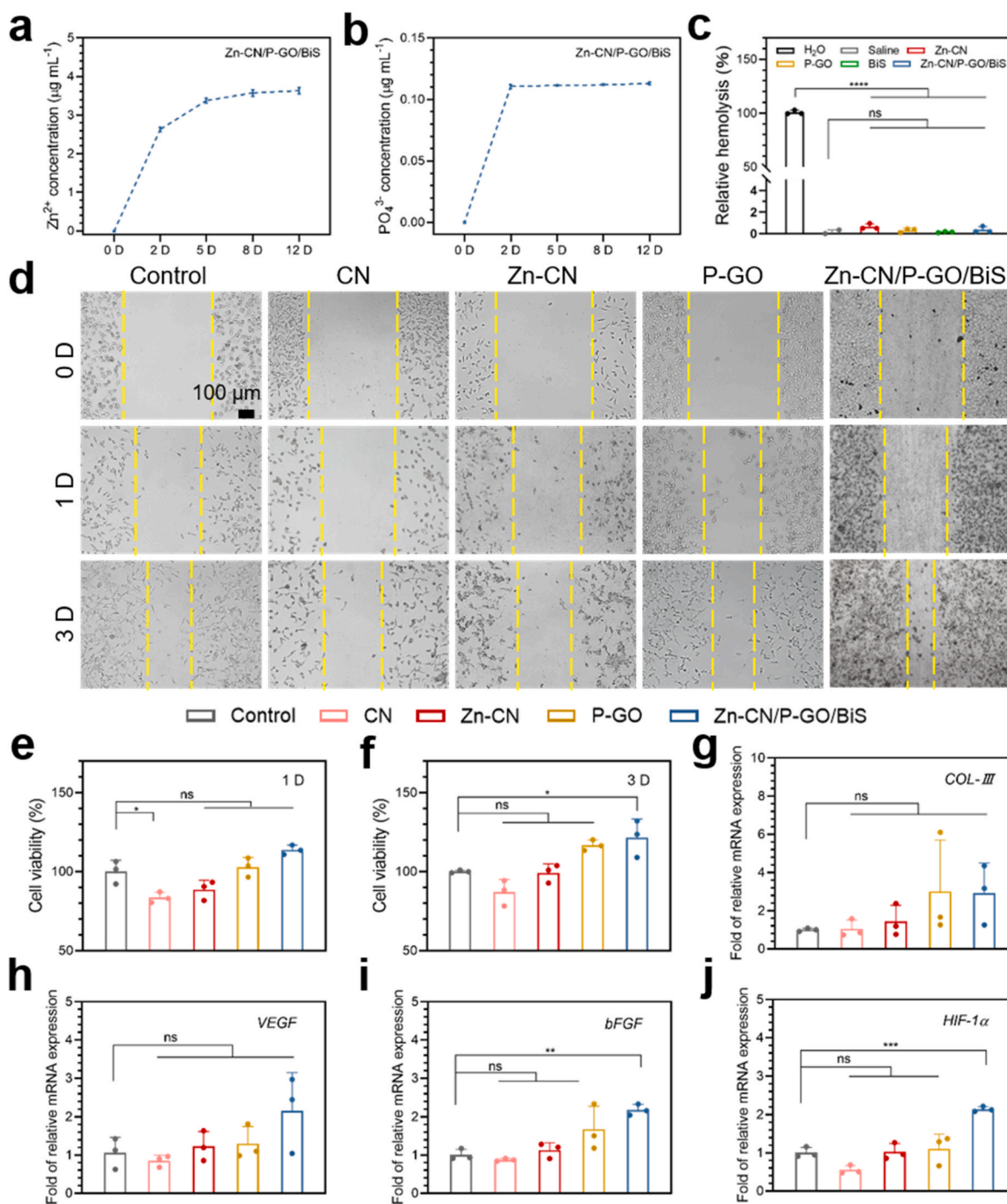


Fig. 5. Cell biocompatibility. Cumulative release of (a) Zn²⁺ and (b) PO₄³⁻ from sample solutions immersed in normal saline at 37 °C for 12 days. (c) Hemolysis ratios of erythrocytes in each group after 4 h of incubation. (d) Cell scratch images of cell migration measured at 0, 1, and 3 days of culture (scale bars, 100 µm). MTT assay to determine the cell viability after (e) 1 and (f) 3 days of co-culture with difference materials. The expression of angiogenesis and epithelialization genes (g) *COL-III*, (h) *VEGF*, (i) *bFGF*, (j) *HIF-1α* in fibroblasts cultured from different materials for 5 days was detected by qRT-PCR.

demonstrated normal cell morphology, with fully spread cytoplasm and extended filopodia. Among the groups, the double-ion group exhibited the highest cell viability and activity, as well as polygonal, lamellar, and filamentous morphologies indicative of its ability to promote cellular growth. In a cell scratch assay, the pipette tip perpendicular to the bottom of the fibroblasts well plate was drawn along the middle on day 0 and co-cultured with the all groups for 1 or 3 days. As shown in Fig. 5d, the cells in the double-ion group showed significant migration and the scratch gap decreased, indicated that cell proliferation was increased in the double-ion group as compared with that in the single-ion groups.

Moreover, the proliferation promotion effect of fibroblasts was more apparent in the double-ion group than single-ion groups. Further quantification of cell viability was undertaken using a 3-(4,5-dimethylthiazol-2-yl)-2,5-diphenyltetrazolium (MTT) colorimetric assay, with cytotoxicity tests conducted for 1 and 3 days. As depicted in Fig. 5e and f, the double-ion group exhibited superior cell viability, reaching 116.81%.

Collagen type III (COL-III) is the main collagen in skin and fascia, and an important protein in the wound healing process [58]. Vascular endothelial growth factor (VEGF) and basic fibroblast growth factor

(bFGF) play important roles in promoting angiogenesis [59]. Hypoxia-inducible factor-1 α (HIF-1 α) lays a key role in cell differentiation and migration [60]. The expression levels of vascular and collagen production-related genes, such as *COL-III*, *VEGF*, *bFGF*, and *HIF-1 α* , were detected by real-time quantitative PCR (qRT-PCR). As shown in Fig. 5g–j, after co-culture with fibroblasts for 5 days, the relative expression levels of these genes were upregulated in the double-ion group as compared with those in the single-ion groups, which proved that the Zn-CN/P-GO/BiS group had more significant effects on tissue repair and related protein deposition.

3.6. *In vivo* wound treatment and biosafety

To further assess the efficacy of the materials in promoting wound healing, tissue regeneration and resistance to infection *in vivo*, a rat wound model of MRSA infection was established. The wound healing process at different times was then assessed (Fig. 6a). The results revealed almost complete healing in the Zn-CN/P-GO/BiS group after 12 days of treatment, with a significantly faster wound healing rate compared to both the control (leave untreated) and 3 M (3 M dressing) groups throughout the entire cycle. Conversely, noticeable defects in wound healing were observed in the control and 3 M groups. To assess the *in vivo* antibacterial efficacy of Zn-CN/P-GO/BiS, we monitored changes in wound temperature in an experimental rat model (Fig. 6b). On day 2 of wound infection, the homogenate of wound tissue was plated on bacterial plates and counted (Fig. 6c and d), and tissue sections

were subjected to Gram staining (Fig. 6e). The results demonstrated that the number of MRSA in the Zn-CN/P-GO/BiS group was significantly lower than that in the control group, which was consistent with our findings from *in vitro* antibacterial experiments. On day 2 of wound infection, bacteria were detected in all the groups, as demonstrated by Gram staining. The highest number of bacteria was detected in the control group. The number of bacteria in the 3 M group was lower than that in the control group. The lowest number of bacteria was detected in the Zn-CN/P-GO/BiS group. On day 5, Zn-CN/P-GO/BiS group bacteria were basically eliminated.

White blood cells (WBCs) and granulocytes are typical inflammatory markers used to screen for the severity of bacterial infections [61]. The therapeutic efficacy of Zn-CN/P-GO/BiS was evaluated *in vivo* by analysing routine blood parameters. The levels of WBCs (Fig. 6f) and granulocytes (Fig. 6g) in the treated group after 12 days were normal, pointing to significant antibacterial activity of Zn-CN/P-GO/BiS *in vivo*. Haematoxylin-eosin (H&E) staining was utilized to evaluate the wound inflammatory response 2, 5, and 12 days after the animal experiment (Fig. 6h). Multiple lobulated neutrophils were observed surrounding the wound site, as indicated by yellow arrows, indicative of a severe bacterial infection. This phenomenon was particularly pronounced in both the control group and 3 M group on day 2. In contrast, the neutrophil count was lower in the Zn-CN/P-GO/BiS group, with relatively mild infection, indicating that Zn-CN/P-GO/BiS had a significant impact on promoting wound healing and tissue regeneration. We performed immunohistochemical staining on day 12 (Fig. 6i), which further

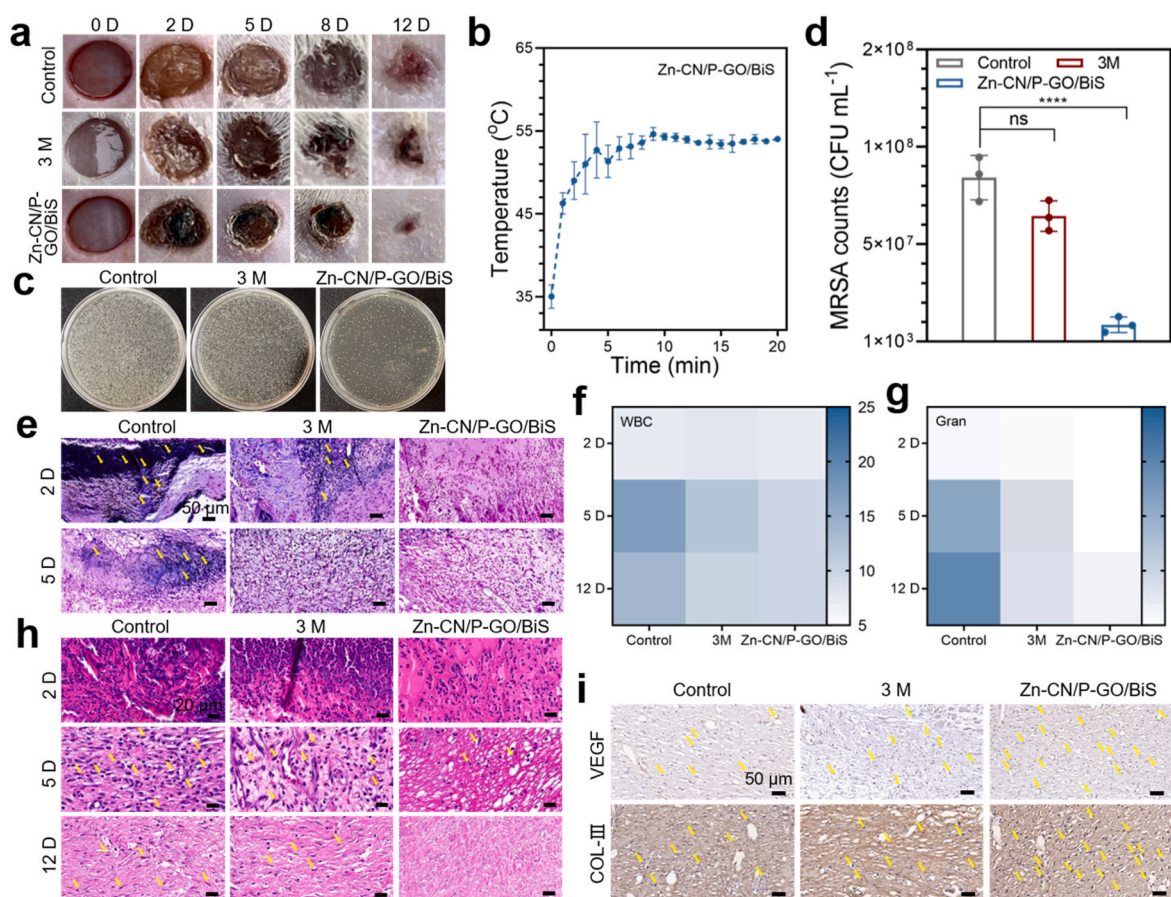


Fig. 6. To evaluate the antibacterial performance, anti-inflammatory, and tissue repair ability of Zn-CN/P-GO/BiS in MRSA infected wounds. (a) Photographs of wounds in the control, 3 M and Zn-CN/P-GO/BiS at 0, 2, 5, 8, and 12 days of treatment. (b) Wound temperature change curve of Zn-CN/P-GO/BiS group rats irradiated with 808 nm NIR for 20 min. (c) Spread plate of homogenate tissue 2 days after wound infection and corresponding (d) MRSA counts. (e) Gram stain images on days 2 and 5 after treatment (scale bars, 50 μ m). (f) WBCs and (g) granulocytes content of the wound at 2, 5, 12 days of treatment (unit: 10^9 L⁻¹). (h) Wound tissue slices of H&E staining images on 2, 5, and 12 days of treatment (scale bars, 20 μ m). (i) Immunohistochemical staining of VEGF and COL-III for wound tissue at day 12, respectively (scale bar, 50 μ m).

revealed that the amounts of VEGF and COL-III (as indicated by yellow arrows) in the Zn–CN/P-GO/BiS group were significantly higher than other groups. Moreover, after 12 days of treatment, histological examination of major organs, including heart, liver, spleen, lung, and kidney, did not reveal any damage or abnormalities (Fig. S22), indicating that Zn–CN/P-GO/BiS is a biocompatible material without toxic side effects *in vivo*.

3.7. Triggered wound healing mechanisms

We further used proteomics to explore the mechanism of wound

repair, and a normal rat wound model was therefore established. The wound healing process at different times was then assessed (Fig. 7a). The results revealed almost complete healing in the Zn–CN/P-GO/BiS group after 12 days of treatment, with a significantly faster wound healing rate compared to the control (leave untreated). We then extracted the healed skin tissue in each group for proteomic analysis. As illustrated in Fig. 7b and c, Pearson's correlation coefficient identification and principal component analysis demonstrated that the quantitative results of the samples exhibited statistical consistency within the groups and significant differences between the groups, indicating that Zn–CN/P-GO/BiS treatment could regulate protein expression. Fig. 7d identified the 312

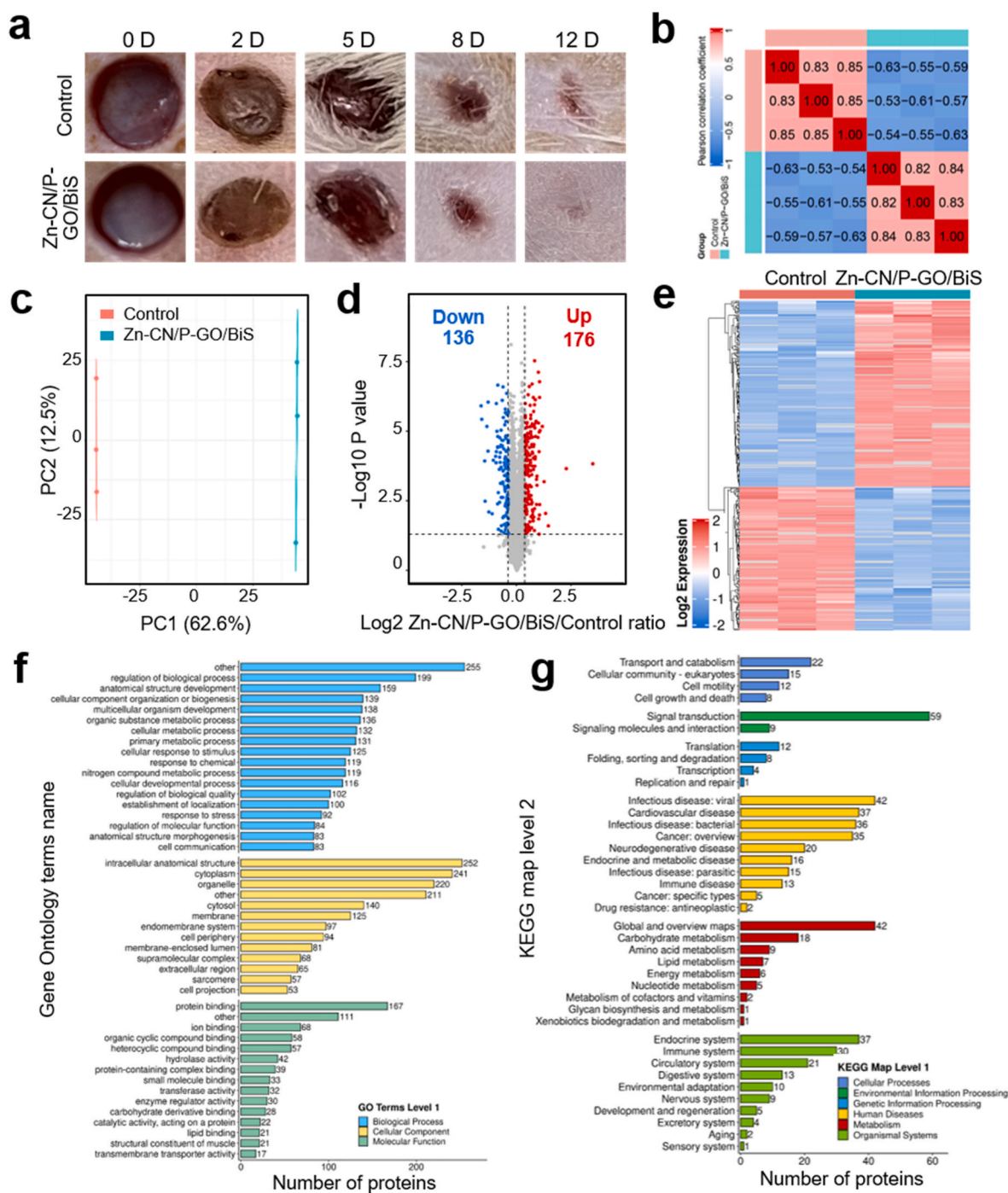


Fig. 7. The overall expression of differential proteins. (a) The wound healing process was evaluated at different times. (b) Pearson's correlation coefficient analysis heat map. (c) Principal component analysis. (d) Volcano plot of differential proteins. (e) Heat map of differential proteins. (f) Gene Ontology secondary classification. (g) KEGG pathway classification.

differentially expressed proteins, with 176 upregulated and 136 down-regulated. The differential protein heat map revealed the relative expression levels of multiple differential proteins after various treatments (Fig. 7e), confirming the protein expression levels determined by Zn-CN/P-GO/BiS. These results suggested that the Zn-CN/P-GO/BiS group exhibited a substantial difference in the number of proteins expressed compared to the control group, potentially including proteins

that promote wound healing. Functional classification statistics of differentially expressed proteins between the two groups were performed using Gene Ontology secondary classification (Fig. 7f) and Kyoto Encyclopedia of Genes and Genomes (KEGG) pathway classification (Fig. 7g). The horizontal axis represents the number of differential proteins in the classification, and the vertical axis represents the secondary functional classification in the primary classification. These

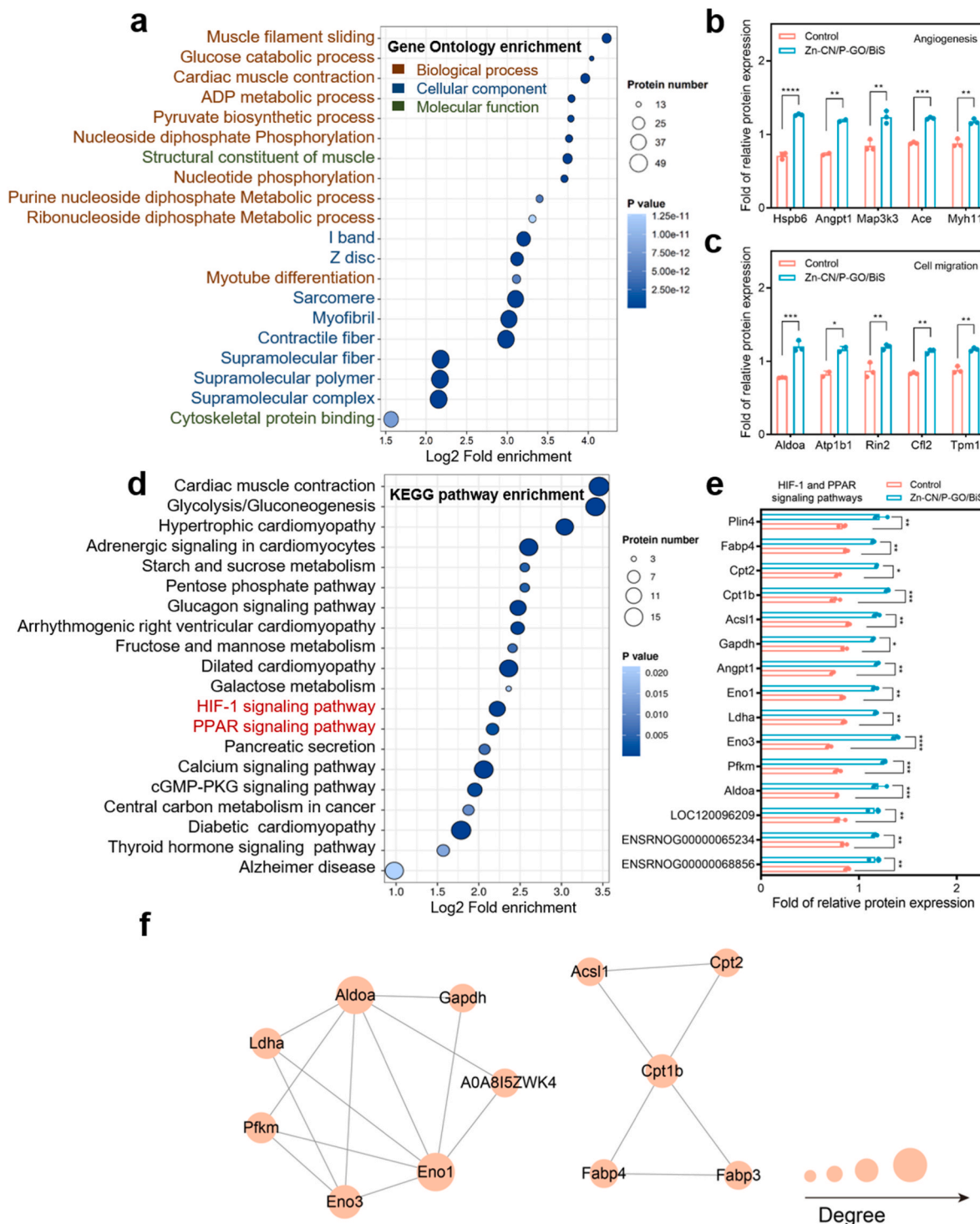


Fig. 8. Exploration of the mechanisms related to wound repair. (a) Dot plot of the top 20 upregulated differential proteins (including biological processes, cellular components, and molecular functions) in Gene Ontology enrichment. Gene Ontology enrichment of upregulated proteins in (b) angiogenesis and (c) cell migration. (d) Dot plot of the top 20 upregulated pathways from KEGG pathway enrichment analysis. (e) Relative expression of upregulated proteins in the HIF-1 and PPAR signaling pathways. (f) PPI network of HIF-1 and PPAR signaling pathways.

include secondary functional classifications of metabolism, genetic information processing, environmental information processing, cellular processes, organismal systems, and human diseases.

We further performed Gene Ontology enrichment analysis of differentially expressed proteins and identified the top 20 most significantly enriched functions that were upregulated (Fig. 8a). The positive regulation of biological processes, cell components and molecular functions mainly included cell metabolism and cell differentiation. More upregulated proteins focused on biological processes, indicating that Zn–CN/P–GO/BiS elevated the metabolic activity of cells. Additionally, the Gene Ontology enrichment we identified focused on upregulated proteins in angiogenesis (Fig. 8b) and cell migration (Fig. 8c). These results implied that Zn–CN/P–GO/BiS regulated the proteins expression in cells, enhancing angiogenic capacity and stimulating cellular repair activity. KEGG pathway enrichment analysis was then performed on differentially expressed proteins, with the top 20 enriched upregulated pathways shown in Fig. 8d. The upregulated proteins within these pathways were mainly enriched in hypoxia-inducible factor (HIF-1) signaling pathway and peroxisome proliferator-activated receptors (PPAR) signaling pathway. These findings indicated that Zn–CN/P–GO/BiS treatment positively enhanced various cellular functions, such as oxygen homeostasis, cell differentiation and migration, and cell metabolism.

Effective skin repair requires dermal adipocyte lipolysis and myofibroblast transformation [62]. Among these activated signaling pathways, the PPAR signaling pathway maintains metabolic homeostasis and regulates lipid metabolism, and the expression of proteins involved in inflammation [63]. PPAR β/δ modulates the inflammatory response of dermal fibroblasts and the proliferation, migration, and adhesion of keratinocytes [64]. PPAR γ regulates the transcription of inflammatory mediators, keratinocyte differentiation, and epidermal keratinization, playing a crucial role in the wound healing process [65]. Healing and regeneration depend on hypoxia-induced signalling. HIF-1, the primary regulator of oxygen homeostasis, modulates various hypoxia-inducible proteins in hypoxic environment and is the upstream pathway of vascular endothelial growth factor (VEGF) signaling pathway [66]. Fig. 8e showed the relative expression of upregulated proteins in the HIF-1 and PPAR signaling pathways. The upregulation of angiopoietin proteins expression promoted angiogenesis, thereby increasing downstream VEGF expression and stimulating angiogenesis. Fig. 8f exhibited the protein–protein interactions (PPI) network of HIF-1 and PPAR signaling pathways. The 12 proteins in the PPI network have robust interactions.

4. Conclusion

In this work, we prepared a Zn–CN/P–GO/BiS ternary heterojunction material that demonstrated excellent antibacterial activity under NIR irradiation. We effectively reduced the band gap of CN through doping and established a heterogeneous interface. The addition of GO accelerated the separation and transfer of the photocatalytic support, and the addition of Zn and P not only effectively constructed the defect and reduced the band gap, but also had certain bactericidal and epithelial-promoting effects. The composite material exhibited not only excellent photothermal performance but also remarkable photocatalytic activity. *In vitro* experiments demonstrated that Zn–CN/P–GO/BiS exhibited an outstanding antibacterial effect (99.60% \pm 0.07%) upon irradiation with NIR light for 20 min, while also exhibiting no cytotoxicity. Furthermore, Zn and P doping promoted tissue regeneration by upregulating fibroblasts proliferation, collagen formation and angiogenesis genes (VEGF, bFGF, HIF-1 α , and COL-III), thereby promoting wound healing. The proteomic analyses reveal that the crafted Zn–CN/P–GO/BiS significantly promoted angiogenesis by upregulating the expression of angiogenic proteins in the hypoxia-inducible factor-1 (HIF-1) signaling pathway, and upregulated the proteins related to anaerobic metabolism to maintain oxygen homeostasis in the wound. In addition, it also promotes the proliferation, migration, and differentiation of

keratinocytes, and keratinization of epidermis by upregulating a variety of proteins related to adipocyte differentiation, lipid metabolism, and inflammatory response in the peroxisome proliferator-activated receptor (PPAR) signaling pathway. Thus, Zn–CN/P–GO/BiS is safe to use *in vivo*. We anticipate that the findings of this work will contribute valuable insights into the field of non-antibiotic therapy.

Ethics approval and consent to participate

The Department of Orthopaedics at Union Hospital, Tongji Medical College, Huazhong University of Science and Technology approved the animal experiments. The animal experiment procedures were performed in accordance with the Animal Management Rules of the Ministry of Health of the P. R. of China and the Guidelines for the Care and Use of Laboratory Animals of China.

CRedit authorship contribution statement

Jin Huang: Writing – review & editing, Writing – original draft, Visualization, Validation, Project administration, Methodology, Formal analysis. **Shuilin Wu:** Writing – review & editing, Visualization, Validation, Supervision, Software, Resources, Project administration, Methodology, Investigation, Funding acquisition, Formal analysis, Data curation, Conceptualization. **Yi Wang:** Writing – review & editing, Validation, Supervision, Data curation. **Jie Shen:** Supervision, Resources, Project administration, Investigation, Funding acquisition. **Chaofeng Wang:** Writing – review & editing, Validation, Supervision, Project administration. **Yufeng Zheng:** Supervision, Resources, Investigation, Funding acquisition. **Paul K. Chu:** Resources, Project administration, Investigation, Funding acquisition. **Xiangmei Liu:** Supervision, Resources, Project administration, Methodology, Investigation, Funding acquisition, Formal analysis, Conceptualization.

Declaration of competing interest

The authors declare no conflict of interest.

Acknowledgements

This work was jointly supported by the National Natural Science Foundation of China (No. 52173251), the China National Funds for Distinguished Young Scientists (No. 51925104), National Natural Science Foundation of China (No. 82002303), Shenzhen Science and Technology Innovation Committee Project, Shenzhen, China (No. SGDX20220530111405038), NSFC-Guangdong Province Joint Program, Guangdong, China (No. U21A2084), the Central Guidance on Local Science and Technology Development Fund of Hebei Province, China (No. 226Z1303G), Yanzhao Young Scientist Project (No. C2023202018) and Beijing Natural Science Foundation (No. 7232338).

Appendix A. Supplementary data

Supplementary data to this article can be found online at <https://doi.org/10.1016/j.bioactmat.2024.03.011>.

References

- [1] B. Li, Y. Luo, Y. Zheng, X. Liu, L. Tan, S. Wu, Two-dimensional antibacterial materials, *Prog. Mater. Sci.* 130 (2022) 100976.
- [2] D.Ş. Karaman, U.K. Ercan, E. Bakay, N. Topaloğlu, J.M. Rosenholm, Evolving technologies and strategies for combating antibacterial resistance in the advent of the postantibiotic era, *Adv. Funct. Mater.* 30 (15) (2020) 1908783.
- [3] L. Serwecińska, Antimicrobials and antibiotic-resistant bacteria: a risk to the environment and to public health, *Water* 12 (12) (2022) 3313.
- [4] C. Mao, W. Jin, Y. Xiang, Y. Zhu, W. Jun, X. Liu, S. Wu, Y. Zheng, K.M.C. Cheung, K.W.K. Yeung, Realizing highly efficient sonodynamic bactericidal capability through the phonon–electron coupling effect using two-dimensional catalytic planar defects, *Adv. Mater.* 35 (9) (2023) 2208681.

- [5] M. Stracy, O. Snitser, I. Yelin, Y. Amer, M. Parizade, R. Katz, G. Rimler, T. Wolf, E. Herzl, G. Koren, J. Kuint, B. Foxman, G. Chodick, V. Shalev, R. Kishony, Minimizing treatment-induced emergence of antibiotic resistance in bacterial infections, *Science* 375 (6583) (2022) 889–894.
- [6] M. Boolchandani, A.W. D'Souza, G. Dantas, Sequencing-based methods and resources to study antimicrobial resistance, *Nat. Rev. Genet.* 20 (6) (2019) 356–370.
- [7] C. Wang, Y. Luo, X. Liu, Z. Cui, Y. Zheng, Y. Liang, Z. Li, S. Zhu, J. Lei, X. Feng, S. Wu, The enhanced photocatalytic sterilization of MOF-based nanohybrid for rapid and portable therapy of bacteria-infected open wounds, *Bioact. Mater.* 13 (2022) 200–211.
- [8] R.Y.K. Chang, S.C. Nang, H.-K. Chan, J. Li, Novel antimicrobial agents for combating antibiotic-resistant bacteria, *Adv. Drug Deliv. Rev.* 187 (2022) 114378.
- [9] J. Fu, X. Liu, Z. Cui, Y. Zheng, H. Jiang, Y. Zhang, Z. Li, Y. Liang, S. Zhu, P.K. Chu, K.W.K. Yeung, S. Wu, Probiotic-based nanoparticles for targeted microbiota modulation and immune restoration in bacterial pneumonia, *Natl. Sci. Rev.* 10 (2023) nwac221.
- [10] Z. Zhou, J. Li, L. Tan, X. Liu, Y. Zheng, Z. Cui, C. Li, K.W.K. Yeung, Z. Li, Y. Liang, S. Zhu, S. Wu, Using tea nanoclusters as β -lactamase inhibitors to cure multidrug-resistant bacterial pneumonia: a promising therapeutic strategy by Chinese materioherbology, *Fundam. Res.* 2 (3) (2022) 496–504.
- [11] Q. Xin, H. Shah, A. Nawaz, W. Xie, M.Z. Akram, A. Batool, L. Tian, S.U. Jan, R. Boddula, B. Guo, Q. Liu, J. Gong, Antibacterial carbon-based nanomaterials, *Adv. Mater.* 31 (45) (2019) 1804838.
- [12] J. Li, C. Wang, S. Wu, Z. Cui, Y. Zheng, Z. Li, H. Jiang, S. Zhu, X. Liu, Superlattice nanofilm on a touchscreen for photoexcited bacteria and virus killing by tuning electronic defects in the heterointerface, *Adv. Mater.* 35 (22) (2023) 2300380.
- [13] Q. Tian, M. Tang, Y. Sun, R. Zou, Z. Chen, M. Zhu, S. Yang, J. Wang, J. Wang, J. Hu, Hydrophilic flower-like CuS superstructures as an efficient 980 nm laser-driven photothermal agent for ablation of cancer cells, *Adv. Mater.* 23 (31) (2011) 3542–3547.
- [14] Y. Li, X. Liu, Z. Cui, Y. Zheng, H. Jiang, Y. Zhang, Y. Liang, Z. Li, S. Zhu, S. Wu, Treating multi-drug-resistant bacterial infections by functionalized nano-bismuth sulfide through the synergy of immunotherapy and bacteria-sensitive phototherapy, *ACS Nano* 16 (9) (2022) 14860–14873.
- [15] P. Rong, S. Gao, S. Ren, H. Lu, J. Yan, L. Li, M. Zhang, Y. Han, S. Jiao, J. Wang, Large-area freestanding Bi₂S₃ nanofibrous membranes for fast photoresponse flexible IR imaging photodetector, *Adv. Funct. Mater.* 33 (24) (2023) 2300159.
- [16] J. Liao, L. Wang, S. Ding, G. Tian, H. Hu, Q. Wang, W. Yin, Molybdenum-based antimicrobial nanomaterials: a comprehensive review, *Nano Today* 50 (2023) 101875.
- [17] Y. Huang, K. Yu, H. Li, K. Xu, Z. Liang, D. Walker, P. Ferreira, P. Fischer, D. L. Emma Fan, Molybdenum disulfide: scalable fabrication of molybdenum disulfide nanostructures and their assembly, *Adv. Mater.* 32 (43) (2020) 2070324.
- [18] Y. Li, C. Liu, X. Cheng, J. Wang, Y. Pan, C. Liu, S. Zhang, X. Jian, PDA-BPs integrated mussel-inspired multifunctional hydrogel coating on PPNK implants for anti-tumor therapy, antibacterial infection and bone regeneration, *Bioact. Mater.* 27 (2023) 546–559.
- [19] L. Tan, J. Li, X. Liu, Z. Cui, X. Yang, S. Zhu, Z. Li, X. Yuan, Y. Zheng, K.W.K. Yeung, H. Pan, X. Wang, S. Wu, Rapid biofilm eradication on bone implants using red phosphorus and near-infrared light, *Adv. Mater.* 30 (31) (2018) 1801808.
- [20] L. Ma, X. Feng, H. Liang, K. Wang, Y. Song, L. Tan, B. Wang, R. Luo, Z. Liao, G. Li, X. Liu, S. Wu, C. Yang, A novel photothermally controlled multifunctional scaffold for clinical treatment of osteosarcoma and tissue regeneration, *Mater. Today Off.* 36 (2020) 48–62.
- [21] W. Li, J. Wang, J. Ren, X. Qu, 3D graphene oxide–polymer hydrogel: near-infrared light-triggered active scaffold for reversible cell capture and on-demand release, *Adv. Mater.* 25 (46) (2023) 6737–6743.
- [22] M. Piksa, C. Lian, I.C. Samuel, K.J. Pawlik, I.D.W. Samuel, K. Matczyszyn, The role of the light source in antimicrobial photodynamic therapy, *Chem. Soc. Rev.* 52 (5) (2023) 1697–1722.
- [23] B. Ezraty, A. Gennaris, F. Barras, J.-F. Collet, Oxidative stress, protein damage and repair in bacteria, *Nat. Rev. Microbiol.* 15 (7) (2017) 385–396.
- [24] L. Jiang, X. Yuan, Y. Pan, J. Liang, G. Zeng, Z. Wu, H. Wang, Doping of graphitic carbon nitride for photocatalysis: a review, *Appl. Catal. B Environ.* 217 (2017) 388–406.
- [25] L. Li, Y. Lu, C. Jiang, Y. Zhu, X. Yang, X. Hu, Z. Lin, Y. Zhang, M. Peng, H. Xia, C. Mao, Actively targeted deep tissue imaging and photothermal-chemo therapy of breast cancer by antibody-functionalized drug-loaded X-ray-responsive bismuth sulfide@ mesoporous silica core–shell nanoparticles, *Adv. Funct. Mater.* 28 (5) (2018) 1704623.
- [26] J. Li, Z. Li, X. Liu, C. Li, Y. Zheng, K.W.K. Yeung, Z. Cui, Y. Liang, S. Zhu, W. Hu, Y. Qi, T. Zhang, X. Wang, S. Wu, Interfacial engineering of Bi₂S₃/Ti₃C₂T_x MXene based on work function for rapid photo-excited bacteria-killing, *Nat. Commun.* 12 (1) (2021) 1224.
- [27] Y. Li, X. Liu, L. Tan, Z. Cui, D. Jing, X. Yang, Y. Liang, Z. Li, S. Zhu, Y. Zheng, K.W. K. Yeung, D. Zheng, X. Wang, S. Wu, Eradicating multidrug-resistant bacteria rapidly using a multi functional g-C₃N₄@ Bi₂S₃ nanorod heterojunction with or without antibiotics, *Adv. Funct. Mater.* 29 (20) (2019) 1900946.
- [28] M. Li, X. Yang, J. Ren, K. Qu, X. Qu, Using graphene oxide high near-infrared absorbance for photothermal treatment of Alzheimer's disease, *Adv. Mater.* 24 (13) (2012) 1722–1728.
- [29] D. Deng, K.S. Novoselov, Q. Fu, N. Zheng, Z. Tian, X. Bao, Catalysis with two-dimensional materials and their heterostructures, *Nat. Nanotechnol.* 11 (3) (2016) 218–230.
- [30] Y. Xiong, H. Li, C. Liu, L. Zheng, C. Liu, J.-O. Wang, S. Liu, Y. Han, L. Gu, J. Qian, D. Wang, Single-atom Fe catalysts for Fenton-like reactions: roles of different N species, *Adv. Mater.* 34 (17) (2022) 2110653.
- [31] C.T. Chasapis, P.-S.A. Ntoupa, C.A. Spiliopoulou, M.E. Stefanidou, Recent aspects of the effects of zinc on human health, *Arch. Toxicol.* 94 (2020) 1443–1460.
- [32] K. Kaur, R. Gupta, S.A. Saraf, S.K. Saraf, Comprehensive reviews in food science and food safety, *Compr. Rev. Food Sci. Food Saf.* 13 (4) (2014) 358–376.
- [33] E. Bafaro, Y. Liu, Y. Xu, R.E. Dempski, The emerging role of zinc transporters in cellular homeostasis and cancer, *Signal Transduct. Tar.* 2 (1) (2017) 1–12.
- [34] J. Ye, B. Li, M. Li, Y. Zheng, S. Wu, Y. Han, Formation of a ZnO nanorods-patterned coating with strong bactericidal capability and quantitative evaluation of the contribution of nanorods-derived puncture and ROS-derived killing, *Bioact. Mater.* 11 (2022) 181–191.
- [35] A. Sirelkhatim, S. Mahmud, A. Seeni, N.H.M. Kaus, L.C. Ann, S.K.M. Bakhori, H. Hasan, D. Mohamad, Review on zinc oxide nanoparticles: antibacterial activity and toxicity mechanism, *Nano-micro Lett.* 7 (2015) 219–242.
- [36] J. Leng, Y. He, Z. Yuan, B. Tao, K. Li, C. Lin, K. Xu, M. Chen, L. Dai, X. Li, T. Huang, K. Cai, Enzymatically-degradable hydrogel coatings on titanium for bacterial infection inhibition and enhanced soft tissue compatibility via a self-adaptive strategy, *Bioact. Mater.* 6 (12) (2021) 4670–4685.
- [37] Z. Tang, N. Kong, J. Ouyang, C. Feng, N.Y. Kim, X. Ji, C. Wang, O.C. Farokhzad, H. Zhang, W. Tao, Phosphorus science-oriented design and synthesis of multifunctional nanomaterials for biomedical applications, *Matter* 2 (2) (2020) 297–322.
- [38] J.W.F. Nicholls, J.P. Chin, T.A. Williams, T.M. Lenton, V. O'Flaherty, J. W. McGrath, On the potential roles of phosphorus in the early evolution of energy metabolism, *Front. Microbiol.* 14 (2023) 1239189.
- [39] W. Liu, A. Dong, B. Wang, H. Zhang, Current advances in black phosphorus-based drug delivery systems for cancer therapy, *Adv. Sci.* 8 (5) (2021) 2003033.
- [40] Ç.Ö. Girit, J.C. Meyer, R. Erni, M.D. Rossell, C. Kisielowski, L. Yang, C.-H. Park, M. F. Crommie, M.L. Cohen, S.G. Louie, A. Zettl, Graphene at the edge: stability and dynamics, *Science* 323 (5922) (2009) 1705–1708.
- [41] F. Banhart, J. Kotakoski, A.V. Krasheninnikov, Structural defects in graphene, *ACS Nano* 5 (1) (2011) 26–41.
- [42] G. Liu, G. Zhao, W. Zhou, Y. Liu, H. Pang, H. Zhang, D. Hao, X. Meng, P. Li, T. Kako, J. Ye, In situ bond modulation of graphitic carbon nitride to construct p–n homojunctions for enhanced photocatalytic hydrogen production, *Adv. Funct. Mater.* 26 (37) (2016) 6822–6829.
- [43] W. Yan, L. Yan, C. Jing, Impact of doped metals on urea-derived g-C₃N₄ for photocatalytic degradation of antibiotics: structure, photoactivity and degradation mechanisms, *Appl. Catal. B Environ.* 244 (2019) 475–485.
- [44] Q. Yin, L. Tan, Q. Lang, X. Ke, L. Bai, K. Guo, R. Qiao, S. Bai, Plasmonic molybdenum oxide nanosheets supported silver nanocubes for enhanced near-infrared antibacterial activity: synergism of photothermal effect, silver release and photocatalytic reactions, *Appl. Catal. B Environ.* 224 (2018) 671–680.
- [45] M. Li, X. Liu, L. Tan, Z. Cui, X. Yang, Z. Li, Y. Zheng, K.W.K. Yeung, P.K. Chu, S. Wu, Noninvasive rapid bacteria-killing and acceleration of wound healing through photothermal/photodynamic/copper ion synergistic action of a hybrid hydrogel, *Biomater. Sci.* 6 (8) (2018) 2110–2121.
- [46] L. Wang, Z. Zhang, X. Xu, L. Yu, T. Yang, X. Zhang, Y. Zhang, H. Zhu, J. Li, J. Zhang, Zn-P bond induced S-scheme heterojunction for efficient photocatalytic tetracycline degradation synergistic H₂ generation, *J. Alloys Compd.* 926 (2022) 166981.
- [47] F. Wei, J. Karges, J. Shen, L. Xie, K. Xiong, X. Zhang, L. Ji, H. Chao, A mitochondria-localized oxygen self-sufficient two-photon nano-photosensitizer for ferroptosis-boosted photodynamic therapy under hypoxia, *Nano Today* 44 (2022) 101509.
- [48] Y. Liu, J. Zhao, X. Xu, Y. Xu, W. Cui, Y. Yang, J. Li, Emodin-based nanoarchitectonics with giant two-photon absorption for enhanced photodynamic therapy, *Angew. Chem. Int. Ed.* 62 (2023) e202308019.
- [49] R. Shen, G. Liang, L. Hao, P. Zhang, X. Li, In-situ synthesis of chemically bonded 2D/2D covalent organic frameworks/O-vacancy WO₃ Z-scheme heterostructure for photocatalytic overall water splitting, *Adv. Mater.* 35 (33) (2023) 2303649.
- [50] C. Mao, W. Zhu, Y. Xiang, Y. Zhu, J. Shen, X. Liu, S. Wu, K.M.C. Cheung, K.W. K. Yeung, Enhanced near-infrared photocatalytic eradication of MRSA biofilms and osseointegration using oxide perovskite-based P–N heterojunction, *Adv. Sci.* 8 (15) (2021) 2002211.
- [51] Z. Tang, W. He, Y. Wang, Y. Wei, X. Yu, J. Xiong, X. Wang, X. Zhang, Z. Zhao, J. Liu, Ternary heterojunction in rGO-coated Ag/Cu₂O catalysts for boosting selective photocatalytic CO₂ reduction into CH₄, *Appl. Catal. B Environ.* 311 (2022) 121371.
- [52] T.F. Krauss, R.M.D.L. Rue, S. Brand, Two-dimensional photonic-bandgap structures operating at near-infrared wavelengths, *Nature* 383 (6602) (1996) 699–702.
- [53] Z. Ya, X. Jiang, P. Wang, J. Cai, Q. Wang, H. Xie, S. Xiang, T. Wang, D. Cai, Template-free synthesis of phosphorus-doped g-C₃N₄ micro-tubes with hierarchical core–shell structure for high-efficient visible light responsive catalysis, *Small* 19 (23) (2023) 2208254.
- [54] B. Wu, Y. Li, K. Su, L. Tan, X. Liu, Z. Cui, X. Yang, Y. Liang, Z. Li, S. Zhu, K.W. K. Yeung, S. Wu, The enhanced photocatalytic properties of MnO₂/g-C₃N₄ heterostructure for rapid sterilization under visible light, *J. Hazard Mater.* 377 (2019) 227–236.
- [55] Y. Wu, J. Li, Z. Shen, D. Wang, R. Dong, J. Zhang, Y. Pan, Y. Li, D. Wang, B. Tang, Double-pronged antimicrobial agents based on a donor- π -acceptor type aggregation-induced emission luminogen, *Angew. Chem. Int. Ed.* 61 (47) (2022) e202212386.

- [56] M.I. Costa, A.B. Sarmiento-Ribeiro, A.C. Gonçalves, Zinc: from biological functions to therapeutic potential, *Int. J. Mol. Sci.* 24 (5) (2023) 4822.
- [57] F. Kus, R.T. Smolenski, M. Tomczyk, Inorganic polyphosphate—regulator of cellular metabolism in homeostasis and disease, *Biomedicines* 10 (4) (2022) 913.
- [58] S.S. Mathew-Steiner, S. Roy, C.K. Sen, Collagen in wound healing, *Bioengineering* 8 (5) (2021) 63.
- [59] T. Asahara, C. Bauters, L.P. Zheng, S. Takeshita, S. Bunting, N. Ferrara, J.F. Symes, J.M. Isner, Synergistic effect of vascular endothelial growth factor and basic fibroblast growth factor on angiogenesis *in vivo*, *Circulation* 92 (9) (1995) 365–371.
- [60] J. You, M. Liu, M. Li, S. Zhai, S. Quni, L. Zhang, X. Liu, K. Jia, Y. Zhang, Y. Zhou, The role of HIF-1 α in bone regeneration: a new direction and challenge in bone tissue engineering, *Int. J. Mol. Sci.* 24 (9) (2023) 8029.
- [61] K. Ley, H.M. Hoffman, P. Kubers, M.A. Cassatella, A. Zychlinsky, C.C. Hedrick, S. D. Catz, Neutrophils: new insights and open questions, *Sci. Immunol.* 3 (30) (2018) eaat4579.
- [62] B.A. Shook, R.R. Wasko, O. Mano, M. Rutenberg-Schoenberg, M.C. Rudolph, B. Zirak, G.C. Rivera-Gonzalez, F. López-Giráldez, S. Zarini, A. Rezza, D.A. Clark, M. Rendl, M.D. Rosenblum, M.B. Gerstein, V. Horsley, Dermal adipocyte lipolysis and myofibroblast conversion are required for efficient skin repair, *Cell Stem Cell* 26 (6) (2020) 880–895. e6.
- [63] A. Christofides, E. Konstantinidou, C. Jani, V.A. Boussiotis, The role of peroxisome proliferator-activated receptors (PPAR) in immune responses, *Metabolism* 114 (2021) 154338.
- [64] A. Magadam, F.B. Engel, Ppar β/δ : linking metabolism to regeneration, *Int. J. Mol. Sci.* 19 (7) (2018) 2013.
- [65] R.L. Konger, E. Derr-Yellin, T.A. Zimmers, T. Katona, X. Xuei, Y. Liu, H.-M. Zhou, E. R. Simpson Jr., M.J. Turner, Epidermal PPAR γ is a key homeostatic regulator of cutaneous inflammation and barrier function in mouse skin, *Int. J. Mol. Sci.* 22 (16) (2021) 8634.
- [66] Y. Huang, Y. Huang, Z. Wang, S. Yu, H. Johnson, Y. Yang, M. Li, J. Li, Y. Deng, K. Liang, Engineered bio-heterojunction with infection-primed H₂S liberation for boosted angiogenesis and infectious cutaneous regeneration, *Small* 19 (45) (2023) 2304324.